

## Review

# Computation-Accelerated Design of Materials and Interfaces for All-Solid-State Lithium-Ion Batteries

Adelaide M. Nolan,<sup>1</sup> Yizhou Zhu,<sup>1</sup> Xingfeng He,<sup>1</sup> Qiang Bai,<sup>1</sup> and Yifei Mo<sup>1,2,\*</sup>

The all-solid-state lithium-ion battery is a promising next-generation battery technology. However, the realization of all-solid-state batteries is impeded by limited understanding of solid electrolyte materials and solid electrolyte-electrode interfaces. In this review, we present an overview of recently developed computation techniques and their applications in understanding and advancing materials and interfaces in all-solid-state batteries. We review the role of *ab initio* molecular dynamics simulations in studying fast ion conductors and discuss the capabilities of thermodynamic calculations powered by materials databases for identifying the chemical and electrochemical stability of solid electrolyte materials and solid electrolyte-electrode interfaces. We highlight the computational studies in the design and discovery of new solid electrolyte materials and outline design guidelines for solid electrolytes and their interfaces. We conclude with discussion of future directions in computation techniques, materials development, and interface engineering for all-solid-state lithium-ion batteries.

## 1. Introduction

The widespread transition to electrified transportation, such as electric vehicles (EVs), requires high-performance electrical energy storage. Lithium-ion batteries (LiBs) have been widely adopted for powering modern EVs. However, current LiBs exhibit safety issues and narrow operating temperature ranges, and further increases in their energy density and charging rate performance are still desired. The all-solid-state battery (ASB) uses a ceramic-based solid electrolyte (SE) to replace a highly flammable, organic electrolyte used in current commercial LiBs (Figure 1). Using SE is a potential solution for resolving the safety issues and improving the energy density and rate performance of LiBs. The ASB is enabled by the breakthrough discovery of Li super-ionic conductors, which provide high  $\text{Li}^+$  conductivities of  $10^{-3}$ – $10^{-2}$  S cm<sup>-1</sup> at room temperature (RT) comparable with the  $\text{Li}^+$  conductivity of commercial liquid electrolyte of LiBs. The  $\text{Li}^+$  super-ionic conductor  $\text{Li}_{10}\text{GeP}_2\text{S}_{12}$  (LGPS) SE enabled ASBs with good cell performance,<sup>1</sup> and an ASB based on  $\text{Li}_{9.54}\text{Si}_{1.74}\text{P}_{1.44}\text{S}_{11.7}\text{Cl}_{10.3}$  (LiSiPSCl) SE exhibited superior performance at high rate and at elevated temperatures.<sup>2</sup> The garnet-structured oxide  $\text{Li}^+$  super-ionic conductor,  $\text{Li}_7\text{La}_3\text{Zr}_2\text{O}_{12}$  (LLZO), enabled the use of a Li metal anode with stable cycling performance.<sup>3</sup> In addition, an all-solid-state thin-film battery based on a LiPON SE with a Li metal anode and a high-voltage  $\text{LiNi}_{0.5}\text{Mn}_{1.5}\text{O}_4$  cathode has been demonstrated with a long cycle life of over 10,000 cycles.<sup>4</sup> As a next-generation LiB technology, ASBs have shown great potential to provide better safety, higher energy density, longer cycle life, higher power rate, and a wider operating temperature range than current commercial LiBs.<sup>5</sup>

## Context & Scale

The realization of successful all-solid-state lithium-ion batteries requires significant research and development in solid electrolyte materials and solid electrolyte-electrode interfaces.

Computational studies play a critical role in providing fundamental understanding and in accelerating the design of new electrolyte materials and interfaces. We review computational techniques, such as *ab initio* molecular dynamics simulations and thermodynamic calculations based on materials databases developed under the Materials Genome Initiative. We demonstrate how these computational techniques are applied to reveal mechanisms of fast ion diffusion in known super-ionic conductors and to predict novel fast lithium-ion conductors. Design principles for fast ionic conductors are summarized.

We review thermodynamic calculations that reveal the intrinsic electrochemical windows of solid electrolytes and experimental techniques that correctly measure the electrochemical stability of solid electrolytes. We summarize the trends in cathodic and anodic stability of materials and the



Several outstanding challenges limit the further improvement of ASBs (Figure 1). First, super-ionic conductor (SIC) materials with  $\text{Li}^+$  ionic conductivities of  $10^{-3}$  S cm $^{-1}$  or higher at RT are a key component of the ASB, but are rare among known materials. Further, many known SICs lack one or a few critical attributes, such as good chemical and electrochemical stability, interface compatibility with high-energy electrodes, or the feasibility for economical large-scale manufacturing and processing. Therefore, significant research effort has been devoted toward discovering, designing, and developing novel SE materials with high ionic conductivity, good stability, and other desirable properties. However, materials development is often time consuming and labor intensive, and is largely reliant on human intuition and serendipity. A computational approach to predict novel materials with desired properties and rational design strategies to guide materials development can significantly accelerate the research and development (R&D) of new SE materials and can shorten trial and error in the laboratory.

Another major challenge for ASBs lies at the interfaces between the SE and electrodes. These solid-solid interfaces can exhibit high interfacial resistance, greatly limiting the overall ASB performance. Various engineering approaches, such as interfacial coatings, have been explored and demonstrated to mitigate performance losses at the interfaces.<sup>6,7</sup> However, detailed atomistic mechanisms at the solid-solid interfaces are difficult to directly characterize in experiments. Computational modeling can complement experiments by providing unique insight into the underlying mechanisms occurring at interfaces in ASBs.

Over the past few years, computational modeling techniques based on first-principles density functional theory (DFT) and on materials databases established under the Materials Genome Initiative (MGI),<sup>8</sup> have been developed for resolving the aforementioned challenges for SEs and interfaces in ASBs. First-principles atomistic modeling can be used to calculate the energies of atomic structures and obtain fundamental understanding of ion transport mechanisms in SIC materials. In addition, first-principles computation can be implemented to predict new materials with little empirical input, as demonstrated for SE materials and for a wide range of materials in batteries, photovoltaics, thermoelectrics, and catalysts.<sup>9–15</sup> The prediction of new materials has been greatly facilitated by the comprehensive materials databases established under the MGI. These databases provide easily accessible thermodynamic data that can be used in calculations for identifying the phase equilibria at different conditions and for quantifying the chemical and electrochemical stability of materials. Furthermore, these computational resources enabled the study of materials interface stability to guide interface engineering for ASBs. Here, we review the recent advancements in computational materials modeling approaches (Section 2) and their contributions toward the fundamental understanding and predictive design of SE materials (Sections 3 and 4) and interfaces (Section 5) in ASBs. We also highlight design principles and strategies developed from computational studies for guiding future R&D of SE materials and interfaces in ASBs.

## 2. Recent Developments in Computational Techniques

First-principles computation methods are based on the fundamental physical principles of quantum mechanics and therefore can be used to calculate materials properties with little experimental input. Since a number of reviews cover first-principles computational methods for battery materials,<sup>16–20</sup> here we focus on recently developed computational techniques, such as *ab initio* molecular dynamics (AIMD) simulations and thermodynamic calculations enabled by materials databases.<sup>21</sup> These new computational techniques are widely used in fundamental studies and in the

guidelines for selecting materials with good stability against lithium metal or under high voltages. Furthermore, we describe how the interphase layer formed is responsible for the compatibility of solid electrolyte with electrodes in all-solid-state batteries. Strategies for designing compatible interfaces in all-solid-state batteries are discussed. Finally, future research directions for computational modeling techniques, new solid electrolytes, comprehensive design principles, and interface engineering are envisioned.

<sup>1</sup>Department of Materials Science and Engineering, University of Maryland, College Park, MD 20742, USA

<sup>2</sup>Maryland Energy Innovation Institute, University of Maryland, College Park, MD 20742, USA

\*Correspondence: [yfmo@umd.edu](mailto:yfmo@umd.edu)

<https://doi.org/10.1016/j.joule.2018.08.017>

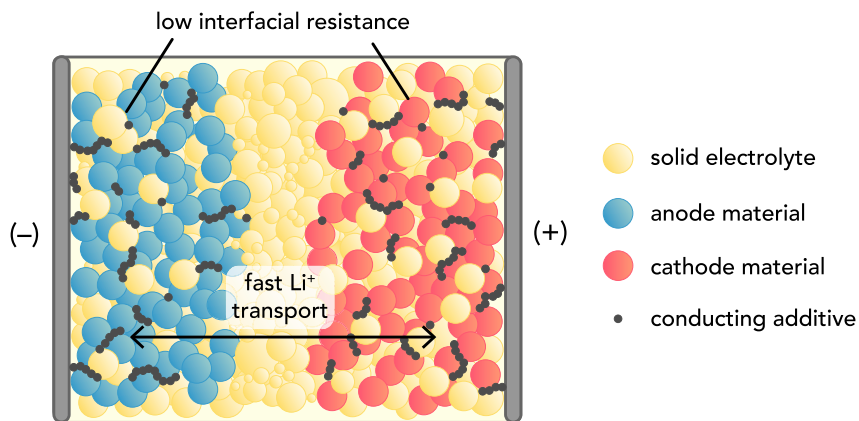


**Figure 1. Schematic Illustration of ASB**

Achieving fast  $\text{Li}^+$  transport within the solid electrolyte and across the interfaces is essential for good ASB performance.

predictive design of SE materials and interfaces in ASBs, providing multiple advantages over previous computational studies.

### 2.1. Ab Initio Molecular Dynamics Simulation

Ion diffusion in materials is often studied using the nudged-elastic-band (NEB) method.<sup>22</sup> NEB calculations are used to obtain the energy barrier and transition state along a particular migration pathway of a mobile ion (usually mediated by a vacancy or interstitial) migrating from one equilibrium site to another. An NEB calculation requires initial and final migration sites and an initial migration pathway as input. In general, NEB calculations are well suited for studying ion diffusion in materials that have well-defined sites and migration pathways. Computational studies based on NEB methods have significantly added to understanding of the static energy landscape of ion migration pathways in electrode and SE materials.<sup>16,23–28</sup> In addition, the diffusion pathway and energy barriers obtained from NEB calculations can be used as input for kinetic Monte Carlo calculations to obtain the overall diffusivity, conductivity, and activation energy in ion-conducting materials with non-dilute carrier concentrations.<sup>29–32</sup>

However, for many SICs, such as LGPS and LLZO, with highly disordered Li-ion sub-lattices, NEB calculations require *a priori* guesses of ion-hopping sites and pathways and so are often more complicated and involved to perform. In studies of SICs, AIMD simulations are performed to directly observe migration events, which are then provided as input for NEB calculations.<sup>33–37</sup> The results from AIMD simulations, together with the energy barriers for specific ion migration pathways from NEB calculations, provide detailed, atomistic-level information on ion diffusion.

In AIMD simulations, the real-time dynamics of all ions in a material are modeled over time. By direct observation of ion dynamics, the details of diffusion mechanisms, such as migration pathways, can be identified.<sup>34</sup> The diffusional properties from AIMD simulations are often quantified as follows.<sup>38,39</sup> The mean-squared displacement (MSD) of a mobile ion (e.g.,  $\text{Li}^+$ ) is a function of the time interval  $\Delta t$  and is given by the expression  $|r_i(t + \Delta t) - r_i(t)|^2$ , where  $r_i(t)$  represents the position of ion  $i$  at time  $t$  in the AIMD simulation. The diffusivity  $D$  of the mobile-ion species is quantified by fitting the Einstein relation,

$$D = \frac{1}{2d\Delta t} \frac{1}{N} \sum_{i=1}^N \langle |r_i(t + \Delta t) - r_i(t)|^2 \rangle, \quad (\text{Equation 1})$$

where  $d = 3$  is the dimension of the system and  $N$  is the number of mobile ions. The angle brackets represent the average over many starting times  $t$  with the same time interval  $\Delta t$ , which is critical for obtaining statistically significant MSD values. The procedure for fitting the Einstein relationship with minimal errors was established in He et al.<sup>39</sup> The ionic conductivity  $\sigma$  is often obtained from the Nernst-Einstein relation,

$$\sigma = \frac{Nq^2}{Vkt} D, \quad (\text{Equation 2})$$

where  $V$  is the total volume of the model and  $q$  is the charge of the mobile-ion species. It should be noted that in [Equation 2](#), the number of mobile ions  $N$  is canceled out by the  $1/N$  in the expression for  $D$  ([Equation 1](#)), so that  $\sigma$  can be directly obtained from the total MSD of all ions with no explicit definition of mobile carriers (e.g.,  $\text{Li}^+$  or vacancy).

As in experimental measurements, the AIMD simulation results, such as diffusivity  $D$  or  $\sigma T$ , obtained for a number of temperatures, can be fitted to an Arrhenius relationship,

$$D = D_0 \exp\left(-\frac{E_a}{kT}\right), \quad (\text{Equation 3})$$

where  $T$  is the temperature and  $k$  is the Boltzmann constant. From this fitting, the pre-exponential factor and the overall activation energy  $E_a$  that reflect all ion migration events are obtained as in experiments. Successful demonstrations of AIMD simulations combined with NEB calculations for identifying diffusion mechanisms, quantifying diffusional properties, and predicting new SICs are reviewed in [Section 3](#).

AIMD simulations have several advantages over other computational techniques. Compared with classical molecular dynamics (MD) simulations, which require force fields that may not be readily available for the candidate material, AIMD simulations are chemically agnostic and are more suitable for studying new materials. In addition, the real-time ion dynamics from AIMD simulations allow direct observation of diffusion mechanisms without the need for *a priori* assumptions of diffusion pathways. AIMD simulations can therefore be used to reveal diffusion modes within materials and to predict new fast ion conductor materials, as shown in [Section 3](#). AIMD simulations can also be used to quantify detailed diffusional information, such as site occupancy, concerted migration, jumping rate, correlation functions, and radial distribution functions, which are not directly accessible via other computation methods but are crucial for understanding ion diffusion.<sup>33,34,40,41</sup> For example, AIMD simulations can be used to directly quantify the pre-exponential factor in the Arrhenius relation ([Equation 3](#)). Recent experimental studies associate a decrease in activation energy with a decrease in the pre-exponential factor and a lower ionic conductivity,<sup>42–45</sup> suggesting that this factor can provide information about ionic conductivity. Therefore, knowledge of the energy barriers alone is inadequate to support claims about high ionic conductivity within a material. AIMD simulations can provide more complete diffusional information in computational studies.

However, the key disadvantage of AIMD simulation is its high computational cost. As a result, AIMD simulations are limited to small supercell models with a few hundred atoms over a very short physical timescale (such as tens of picoseconds to a few nanoseconds). Since ion diffusion is a stochastic process at the atomistic scale, sampling a sufficient number of ion migration events during an AIMD simulation is crucial for obtaining accurate diffusional properties.<sup>39</sup> For this reason, AIMD simulations are limited to studying materials with high ionic conductivity, and are often performed at high temperatures, typically 600 K or higher, so that a large number of diffusional

events can be observed and sampled during the short physical time span of the simulation. Mo and co-workers established a scheme to quantify the statistical variance of calculated diffusional properties from the total number of diffusional events observed in AIMD simulations.<sup>39</sup> From these analyses, it was found that even for current state-of-the-art AIMD simulations, the error bound of extrapolated RT ionic conductivity can be as large as two orders of magnitude.<sup>39</sup> This error in the extrapolated ionic conductivity can be significantly larger if fewer data points are used to fit the Arrhenius plot, fewer ion migration events are sampled, and if the fitting procedures are improperly performed.<sup>39</sup>

AIMD simulation results can deviate in other ways from experiment. The diffusion mechanisms at the high temperatures in AIMD simulations may not be identical to those at RT, which may cause discrepancies between computational and experimental values of diffusion properties. For example, in LLZO, the ordering and site occupancy of the mobile-ion sublattice may vary with temperature.<sup>46–48</sup> Calculating ionic conductivity using the Nernst-Einstein relationship (Equation 2) based on self-diffusivity  $D$  is applicable to materials with dilute and isolated mobile carriers. Since the ion hoppings in many fast ion conductor materials are strongly correlated,<sup>34</sup> the quantification of ionic conductivity should consider the correlation factor, such as the Haven ratio. In addition, the total activation energy fitted from the AIMD simulations may or may not fully capture the formation energy of mobile carriers. This formation energy of mobile carriers may be significant for pristine, non-doped materials with highly ordered Li sublattices, and should be carefully evaluated and considered as a part of the total activation energy.<sup>49–53</sup> As a final note, computational results are based on bulk single crystals, and experimentally measured values of diffusional properties are affected by impurity phases, grain boundaries and microstructure, and local variations in composition resulting from synthesis and processing conditions. All the caveats described above should be considered when drawing a quantitative comparison between computational and experimental results.

## 2.2. Thermodynamic Calculations Enabled by Computational Materials Database

The foundation of computational materials databases such as the Materials Project (MP),<sup>21</sup> Automatic Flow (AFLOW),<sup>54</sup> and the Open Quantum Materials Database (OQMD),<sup>55</sup> which compile the DFT energies of known inorganic compounds, is a major achievement of the MGI.<sup>8</sup> From these databases, the energies and properties of thousands of materials are easily accessible. The reaction energy between any materials in the database can be obtained, and the phase diagram of any compositional system can be constructed. By harnessing these new databases, thermodynamic calculation approaches have been established to evaluate phase stability (Section 2.2.1), chemical and electrochemical stability (Section 2.2.2) of materials, and the equilibria at materials interfaces (Section 2.2.3).

**2.2.1. Phase Stability of Materials.** An energy convex hull is constructed by using the energies of all the compounds in the compositional space, as obtained from a materials database.<sup>56</sup> This energy convex hull can be used to quantify the thermodynamic phase stability of materials. The energy above hull of a compound,  $E_{\text{hull}}$ , is obtained by comparing the compound's energy with the energy convex hull, and corresponds to the absolute value of the decomposition energy of the compound at its thermodynamic phase equilibria (Figure 2A). A compound with  $E_{\text{hull}} = 0$  lies on the energy convex hull and is a thermodynamically stable phase at 0 K. A compound with  $E_{\text{hull}} > 0$  is thermodynamically metastable, and a material with a high energy above hull (e.g., >100 meV/atom) may have a strong thermodynamic driving force for decomposition and may be difficult to synthesize.<sup>57</sup> Therefore,

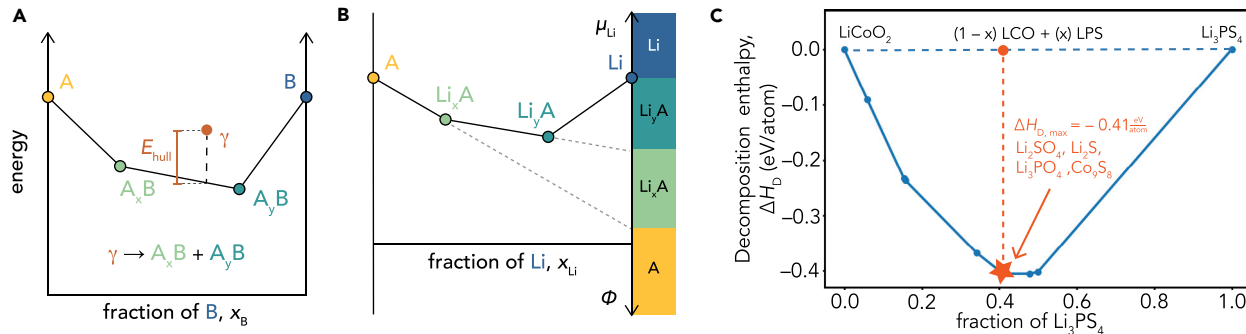


**Figure 2. Schematic Illustrations of Thermodynamic Calculations**

- (A) Schematic of an energy convex hull, indicating the energy above hull  $E_{\text{hull}}$  of a metastable  $\gamma$  phase and its decomposition reaction into the phase equilibria.
- (B) Schematic of a GPPD, illustrating the evolution of phase equilibria under changing Li chemical potential  $\mu_{\text{Li}}$  and an applied voltage  $\phi$ .
- (C) Mutual reaction energy versus composition of a pseudo-binary composed of  $\text{LiCoO}_2$  and  $\text{Li}_3\text{PS}_4$ . The star corresponds to the predicted phase equilibria with decomposition enthalpy  $\Delta H_D$  at the mixing ratio.

$E_{\text{hull}}$  is often used as a simplified quantitative metric to evaluate the phase stability of a material.

Computational studies have used this  $E_{\text{hull}}$  metric in the successful prediction of multiple new SE materials (Sections 3.2 and 3.3). It should be noted that many compounds with a high  $E_{\text{hull}}$  (i.e., less stable compared with the phase equilibria) may nevertheless exhibit highly negative formation energies from their elementary state reactants. Thus, this formation energy of a compound is not suitable for describing the compound's phase stability. Analyses of phase stability should be included in computational studies predicting new materials, since the materials with poor phase stability may be less experimentally feasible. Examples of computational prediction are provided in Section 3.3.

The limitations of DFT calculations should be considered when interpreting analyses of phase stability. First, DFT calculations are based on static energy at 0 K, which neglects the entropy  $S$  and the  $PV$  term, instead of on Gibbs free energy. Since most analyses of materials stability examine the reaction energies between solid phases, it is reasonable to assume that the differences of  $TS$  and  $PV$  terms between solid phases are small at standard conditions. However, the highly disordered mobile-ion sublattice in fast ion conductor materials may exhibit significantly higher configurational entropy than other solid phases. SICs such as LGPS and LLZO were reported to be entropically stabilized at elevated synthesis temperatures.<sup>38,58</sup> Monte Carlo simulations based on a cluster expansion Hamiltonian have been used to quantify the configurational entropy of materials at finite temperatures.<sup>16,36</sup> In addition, the vibrational entropy can be quantified by DFT phonon calculations.<sup>59,60</sup> Often, these types of analyses of entropic effects are not included in studies of phase stability due to their high computational cost. In addition to the aforementioned sources of error, the interpretation of materials stability should also properly consider the energy errors from DFT calculations.<sup>16,61</sup>

**2.2.2. Materials Stability as a Function of External Conditions.** The grand potential phase diagram (GPPD) was developed to evaluate the stability of materials as a function of external conditions, such as applied potential or  $\text{O}_2$  partial pressure.<sup>56,62</sup> A GPPD describes a system that is open to one or more external components.<sup>56</sup> Using a GPPD, the stability of a phase can therefore be assessed as a function of

external conditions such as chemical potential (e.g.,  $\mu_O$  or  $\mu_{Li}$ ) or applied potential  $\varphi$ . In LiBs,<sup>62–64</sup> the equilibrium under an applied potential  $\varphi$  referenced to Li metal  $\mu_{Li}^0$  can be described by an equilibrium at Li chemical potential

$$\mu_{Li}(\varphi) = \mu_{Li}^0 - e\varphi. \quad (\text{Equation 4})$$

Therefore, the GPPD evaluated with respect to  $\mu_{Li}$  describes the electrochemical lithiation and delithiation of materials under applied potential  $\varphi$  (Figure 2B). The cathodic and anodic limits of a material are the potentials at which the reduction and the oxidation reactions become thermodynamically favorable, respectively (Section 4). The electrochemical window is the gap between the reduction and oxidation potentials based on the Gibbs free energy difference of the reactants and products, and is different from the band gap or the gap between the levels of highest occupied molecular orbital (HOMO) and lowest unoccupied molecular orbital (LUMO).<sup>65</sup> The proper alignment of HOMO and LUMO levels is only a necessary condition of the electrochemical stability. Computational studies have shown that the gap between HOMO and LUMO is an upper bound of the electrochemical window.<sup>66,67</sup> The GPPD approach is also applied to study the thermal stability of electrode materials, such as oxygen evolution at high temperatures.<sup>33,68</sup>

**2.2.3. Thermodynamic Equilibria at Interfaces.** Atomistic modeling of interfaces is challenging due to the technical difficulties of constructing and calculating interface models. Using the computational materials database, the thermodynamic calculations for materials stability (Sections 2.2.1 and 2.2.2) can also be applied to evaluate the thermodynamic equilibrium of two materials in contact. These calculations of interface equilibria were proposed and described in previous studies.<sup>69–71</sup> The thermodynamic equilibrium of two mixing materials can be determined from the phase diagram comprising all the elements in these two materials using the materials database. If the phase equilibria contain phases other than the two original materials, these two materials are not in equilibrium with each other, and may react exothermically to form other phases (Figure 2C); for example, their phase equilibria or other kinetically preferred phases. This calculation therefore identifies the chemical stability of two materials at their interface. Similarly, GPPDs can also be used to evaluate the equilibrium between two materials in contact under an applied potential, which is the electrochemical stability of the interface.

For SEs and electrodes commonly used for ASBs, these phase diagrams are high dimensional in composition (e.g., quaternary or beyond) and involve a large number of compounds, which often do not have experimentally measured energies. These thermodynamic calculations could not be performed before the advent of computational materials databases due to the lack of thermodynamic data for a large number of materials. As enabled by computational materials databases, these thermodynamic calculations are now performed with low computational cost and have led to significant understanding of solid interfaces in ASBs. These thermodynamic calculations using computational databases are a major advancement achieved under the MGI and have accelerated the study, design, and discovery of new materials and interfaces, as reviewed in Sections 4 and 5.

### 3. Computational Study and Design of Solid Electrolytes

#### 3.1. Ion Diffusion Mechanism in Super-Ionic Conductors

The high  $Li^+$  conductivity of  $10^{-3}$  to  $10^{-2} \text{ S cm}^{-1}$  at RT exhibited in SIC materials such as LGPS, garnet LLZO, and NASICON  $Li_{1.3}Al_{0.3}Ti_{1.7}(PO_4)_3$  (LATP), is a crucial

property for their application as SEs in ASBs. Since such high ionic conductivity is unique among solid materials, understanding the fast Li<sup>+</sup> diffusion mechanisms in SICs is important for future design and discovery of novel SEs for ASBs.

AIMD simulation was demonstrated by Mo et al.<sup>38</sup> as an effective technique for revealing atomic-level mechanisms of ion diffusion and for quantifying diffusional properties in fast ion conductors. The diffusivity, ionic conductivity, and activation energy ( $E_a$ ) calculated from AIMD simulations have achieved excellent agreement with the experiments for many SIC materials, including LGPS, LLZO, and LATP.<sup>23,34,38,39,62,70</sup> For example, a Li<sup>+</sup> ionic conductivity of 10–14 mS cm<sup>-1</sup> and an activation energy  $E_a$  of 0.20–0.24 eV in LGPS calculated using AIMD simulations<sup>34,38,39,62</sup> are in agreement with experimental values of 12 mS cm<sup>-1</sup> and 0.24 eV,<sup>1</sup> respectively. These diffusional properties are difficult to obtain from NEB calculations, which only provide the migration energy barrier for specific migration pathways and do not provide ionic conductivity or the pre-exponential factor in the Arrhenius relation (Equation 3).

In addition, the dynamics of ions from AIMD simulations provide direct observation of ion-hopping mechanisms and diffusion pathways. Kamaya et al. initially proposed that LGPS conducts Li ions in a one-dimensional (1D) pathway along the c axis.<sup>1</sup> The AIMD simulation study by Mo et al. confirmed the fast Li<sup>+</sup> diffusion along this 1D c channel and observed Li<sup>+</sup> diffusion in the ab plane with significantly lower diffusivity, indicating anisotropic three-dimensional (3D) Li<sup>+</sup> conduction in the LGPS structure (Figures 3A and 3B).<sup>38</sup> This 3D diffusion mechanism was later confirmed in neutron powder diffraction experiments by Weber et al.<sup>72</sup> (Figures 3C and 3D). In addition, MD simulations also uncovered a previously overlooked Li4 site in the LGPS structure,<sup>73</sup> which was later confirmed in neutron diffraction experiments.<sup>74</sup> These results demonstrate the accuracy of AIMD simulations for predicting the potential energy surface of ions in crystal structures.

Moreover, by visualizing ion dynamics with femtosecond time resolution, AIMD simulations revealed the concerted migration of multiple ions in many SICs (Figures 3E and 3F).<sup>34</sup> During concerted migration, multiple Li ions hop to the nearest sites within a time frame on the order of 1 ps, in contrast to the isolated hopping of individual ions in typical solids. Consistent with earlier AIMD simulations reporting concerted migration in LGPS<sup>75</sup> and LLZO,<sup>37</sup> He et al. confirmed the atomistic mechanism of concerted migration occurred in several SIC materials with a variety of structures, and demonstrated that the concerted migration of multiple ions is a general phenomenon among SIC materials.<sup>34</sup> Concerted migration was confirmed as a diffusion mechanism in several newly discovered SICs, including LiZnPS<sub>4</sub>, Na<sub>10</sub>SnP<sub>2</sub>S<sub>12</sub>, and LiTaSiO<sub>5</sub>.<sup>34,36,76</sup>

Computational modeling by Mo and co-workers also revealed the mechanistic origin of multiple-ion concerted migration, which is crucial for understanding fast ion conduction in SICs.<sup>34</sup> SIC materials, e.g., LLZO and LATP, have two Li sites with different site energies (Figure 4B), and some Li ions occupy sites with higher energy as a result of the high Li concentrations and strong Li-Li Coulomb interactions in these materials.<sup>34</sup> During concerted migration, while some Li ions climb up the energy landscape, the other Li ions occupying the high-energy sites migrate down from these sites and decrease their energies, and these decreases in energy cancel out part of the total migration energy barrier (Figure 4A). As a result, concerted migration of multiple ions in such ion configurations leads to a lower overall migration barrier than that of single-ion migration. The discovery and understanding of concerted

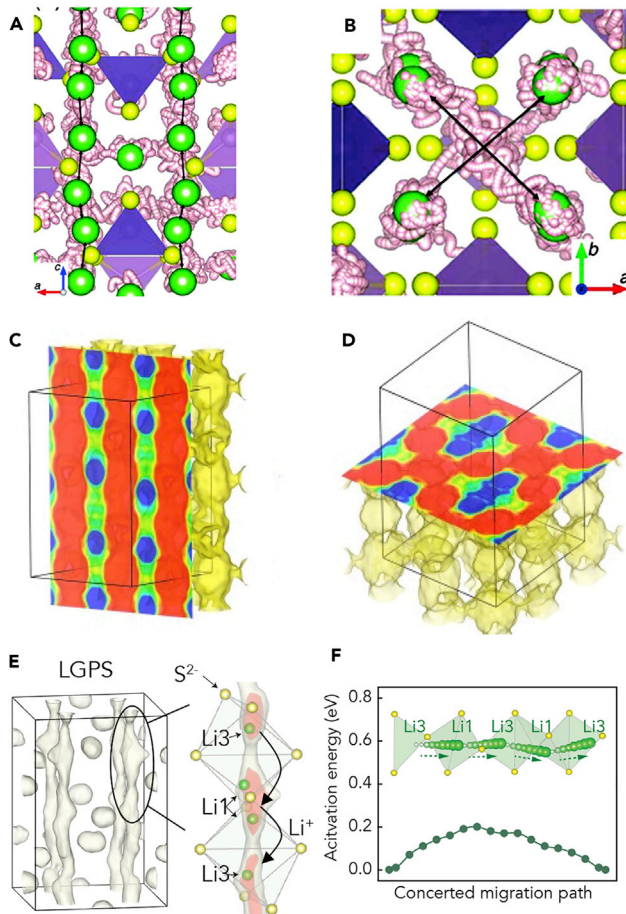


**Figure 3. Li-Ion Diffusion Pathways in LGPS**

(A and B) The trajectory of Li ions (white) from AIMD simulations, showing Li<sup>+</sup> diffusion pathways (A) in the *c* channel and (B) in the *ab* plane. Reproduced from Mo et al.<sup>38</sup> with permission. Copyright 2013, American Chemical Society.

(C and D) Nuclear density maps reconstructed by the maximum entropy method from neutron diffraction analyses, showing the diffusion pathway of Li ions in the (C) <001> and (D) <110> directions. Reproduced from Weber et al.<sup>72</sup> with permission. Copyright 2016, American Chemical Society.

(E) Probability density of Li ions from AIMD simulations, showing agreement with neutron diffraction analyses (C and D).

(F) Energy profile calculated using NEB method of concerted migration of multiple Li ions along the 1D *c* channel diffusion pathway in LGPS. Reproduced from He et al.<sup>34</sup> with permission. Copyright 2017, Nature Publishing Group.

migration mechanisms in SICs highlights the advantage of computational modeling in revealing atomic-scale diffusion mechanisms.

### 3.2. Design Principles for Fast Ion Conductors

The characteristics that promote fast ion conduction in materials have been summarized based on the observations of known fast ion conductors.<sup>77,78</sup> In general, in materials with more polarizable anions, the mobile cations migrate with a lower migration barrier. Therefore, sulfides generally exhibit a lower Li<sup>+</sup> migration energy barrier than oxides with the same crystal structural framework.<sup>23</sup> In addition, the crystal structure framework formed by the immobile lattice should have open, interconnected diffusion channels with large diameters. The

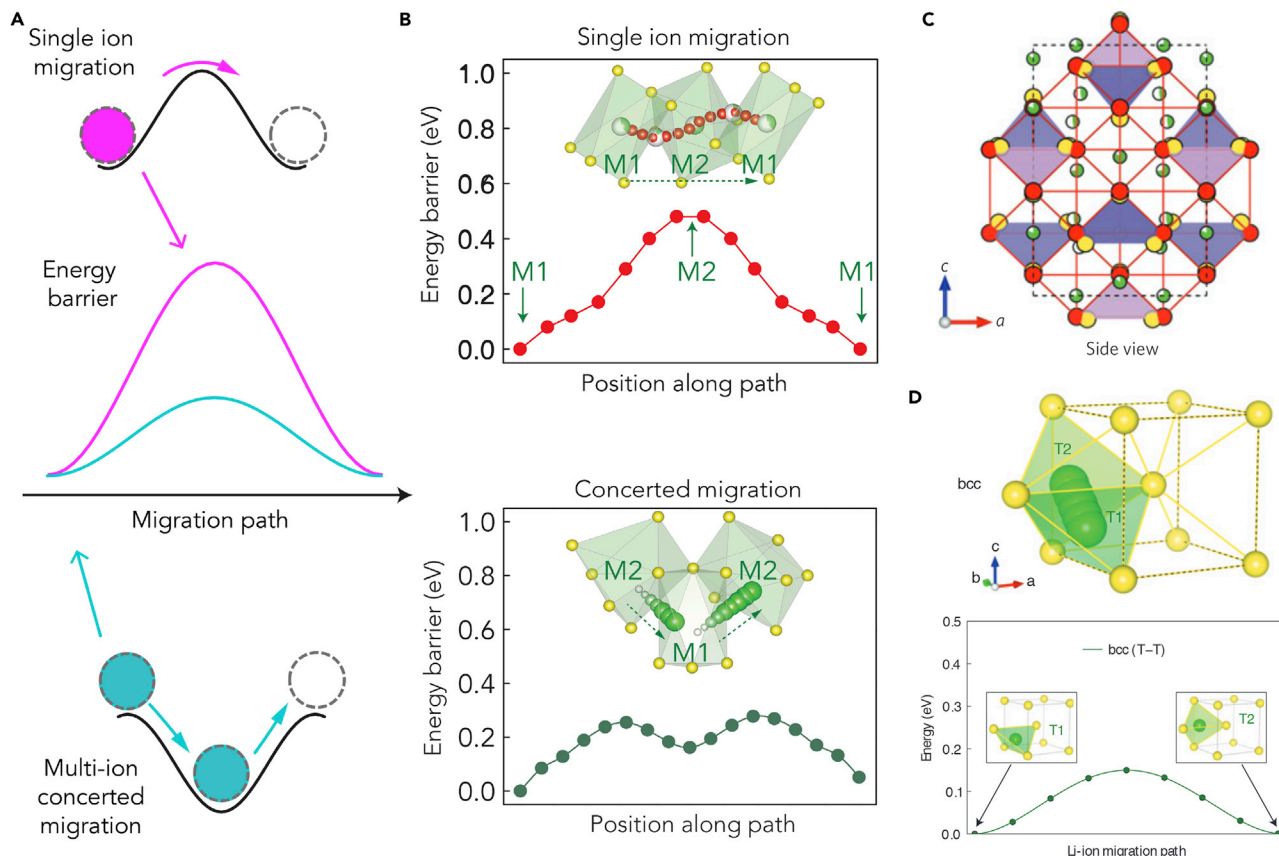


**Figure 4. Diffusion Mechanisms in Super-Ionic Conductors**

(A) Illustration of energy profiles for single-ion migration (pink) versus multiple-ion concerted migration (blue). Reproduced from He et al.<sup>34</sup> with permission. Copyright 2017, Nature Publishing Group.

(B) Energy landscape of single  $\text{Li}^+$  migration (upper) and the energy barrier of concerted migration (lower) in LATP, as calculated using the NEB method. Reproduced from He et al.<sup>34</sup> with permission. Copyright 2017, Nature Publishing Group.

(C) S anion sublattice (yellow circles) in LGPS compared with the bcc structure (red circles). Li atoms,  $\text{PS}_4$  tetrahedra, and  $\text{GeS}_4$  tetrahedra are colored green, purple, and blue, respectively. Reproduced from Wang et al.<sup>23</sup> with permission. Copyright 2015, Nature Publishing Group.

(D) Li-ion migration path and calculated migration energy in a bcc S-anion sublattice. Reproduced from Wang et al.<sup>23</sup> with permission. Copyright 2015, Nature Publishing Group.

material should also have a high concentration of mobile Li-ion carriers, usually existing as vacancies or interstitials in typical solids. In SICs, a disordered mobile Li-ion sublattice with a large number of partially occupied sites exhibits a significant fraction of sites available for hopping, leading to a high mobile carrier concentration. Overall, low migration barrier and high carrier concentration are prerequisites for high ionic conductivity, as given by the Nernst-Einstein relation (Equation 2).

Design principles are established with respect to the coordination and topology of Li sites in the structural framework. First-principles computation by Ceder and co-workers compared the  $\text{Li}^+$  migration energy landscape for different anion sublattice structures and found that materials with a body-centered cubic (bcc) anion sublattice exhibited the lowest  $\text{Li}^+$  migration barrier.<sup>23</sup> In a bcc anion sublattice, the anions form face-sharing tetrahedra, and Li ions migrate between these tetrahedral sites (Figure 4D). This migration pathway has a low energy barrier of approximately 0.2 eV in a  $\text{S}^{2-}$  sublattice with a typical anion packing density of Li-containing

sulfides. LGPS and Li<sub>7</sub>P<sub>3</sub>S<sub>11</sub> were also found to have S<sup>2-</sup> packing closely resembling a bcc framework (Figure 4C), explaining the low migration barrier and high ionic conductivity in these two materials. Other anion frameworks, such as the face-centered cubic (fcc) and hexagonal close-packed (hcp) sublattices, in which Li<sup>+</sup> migrates through an intermediate octahedral site between tetrahedral sites, exhibit significantly higher energy barriers for Li<sup>+</sup> migration than the bcc lattice. As a result, the use of an anion sublattice resembling a bcc framework was established as a design principle for fast ion conductors. Using this design principle, Ceder and co-workers discovered a new SIC, Li<sub>1+2x</sub>Zn<sub>1-x</sub>PS<sub>4</sub> ( $x = 0\text{--}0.75$ ) based on the structure of LiZnPS<sub>4</sub>, which has a S<sup>2-</sup> framework close to bcc. The Li ionic conductivity of Li<sub>1+2x</sub>Zn<sub>1-x</sub>PS<sub>4</sub> was calculated to be on the order of 10<sup>-2</sup> S cm<sup>-1</sup> at RT for  $x = 0.25\text{--}0.75$ .<sup>36</sup> These materials were synthesized by multiple experimental groups and were confirmed to be fast Li-ion conductors with RT ionic conductivities on the order of 10<sup>-4</sup>–10<sup>-3</sup> S cm<sup>-1</sup> for  $x = 0.5\text{--}0.8$ .<sup>79,80</sup> The quantitative discrepancy between the ionic conductivities obtained from computation and those found in experiments was attributed to the poor crystallinity of the synthesized Li<sub>1+2x</sub>Zn<sub>1-x</sub>PS<sub>4</sub> samples and the impurity phases, such as amorphous Li<sub>3</sub>PS<sub>4</sub> and Li<sub>4</sub>P<sub>2</sub>S<sub>6</sub>, formed during synthesis.<sup>79,80</sup>

Since the bcc anion framework is rare among Li-containing sulfides and oxides, a design principle based on the concerted migration mechanism was proposed to decrease activation energy in materials with non-bcc anion framework. As proposed by Mo and co-workers, inserting extra Li ions into high-energy sites through aliovalent doping may activate concerted migration in the material and hence reduce the overall migration barrier.<sup>34</sup> With first-principles computation, this design strategy was demonstrated by using Zr substitution to convert LiTaSiO<sub>5</sub>, a poor Li-ion conductor, into Li<sub>1.25</sub>Ta<sub>0.75</sub>Zr<sub>0.25</sub>SiO<sub>5</sub>, a fast ion conductor with RT conductivity on the order of 10<sup>-3</sup> S cm<sup>-1</sup> and an  $E_a$  of 0.23 ± 0.01 eV.<sup>34</sup> This design principle based on the concerted migration mechanism is a promising route for the future design and development of new SICs.

The aforementioned design principles largely emphasize lowering the migration energy barrier. However, other factors, such as the pre-exponential factor of the Arrhenius relation, are also critical to achieve a high ionic conductivity. The pre-exponential factor is related to many factors, including anion polarizability, lattice softness, mobile carrier concentration, and the ordering of the mobile-ion sublattice,<sup>42–45</sup> but design principles that consider these factors have not yet been developed. At the current stage, first-principles computation is required to identify the dopant and exact composition for a particular crystal structural framework to design a fast Li-ion conductor (Section 3.3).

### 3.3. Design of New Materials from First-Principles Computation

First-principles computation has been successfully demonstrated in the prediction of new SIC materials. For example, Ceder and co-workers predicted two substituted variants of LGPS, Li<sub>10</sub>SiP<sub>2</sub>S<sub>12</sub> and Li<sub>10</sub>SnP<sub>2</sub>S<sub>12</sub>, in which the expensive Ge in LGPS was replaced with cheaper, more abundant Si and Sn, respectively.<sup>62</sup> The new Li<sub>10</sub>SiP<sub>2</sub>S<sub>12</sub> and Li<sub>10</sub>SnP<sub>2</sub>S<sub>12</sub> compounds had low calculated  $E_{\text{hull}}$  values of less than 20 meV/atom (Figure 5B), comparable with that of LGPS, suggesting these predicted compounds had good phase stability and the potential to be synthesized.<sup>62</sup> Consistent with computational predictions, Li<sub>10</sub>SnP<sub>2</sub>S<sub>12</sub> and Li<sub>10</sub>SiP<sub>2</sub>S<sub>12</sub>, along with its variant Li<sub>10+x</sub>Si<sub>1+x</sub>P<sub>2-x</sub>S<sub>12</sub> ( $x = 0.20\text{--}0.43$ ),<sup>81</sup> have been successfully synthesized in multiple experimental studies.<sup>81–84</sup> The  $E_{\text{hull}}$  can also be used as a metric to exclude candidate compounds with poor phase stability. For example, the

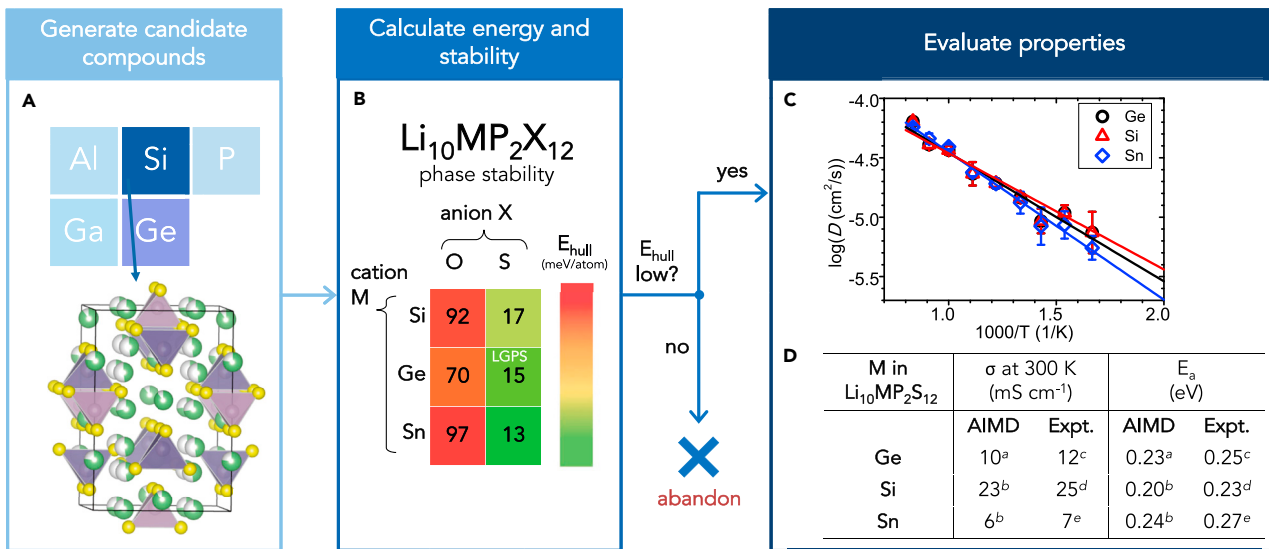


**Figure 5. Schematic Workflow of Computational Materials Design**

(A) Generate new candidate compounds  $\text{Li}_{10}\text{MP}_2\text{X}_{12}$  ( $\text{M} = \text{Si}, \text{Ge}, \text{Sn}, \text{X} = \text{O}, \text{S}$ ) by elemental substitution of LGPS.

(B) Calculate phase stability of  $\text{Li}_{10}\text{MP}_2\text{X}_{12}$  candidate compounds using  $E_{\text{hull}}$  and abandon unstable candidates.

(C and D) Calculate properties of predicted stable materials. (C) Arrhenius plot of  $\text{Li}^+$  diffusivity of  $\text{Li}_{10}\text{SiP}_2\text{S}_{12}$  and  $\text{Li}_{10}\text{SnP}_2\text{S}_{12}$  compared with LGPS, from AIMD simulations. Reproduced from Ong et al.<sup>62</sup> with permission. Copyright 2012, Royal Society of Chemistry. (D)  $\text{Li}^+$  conductivities and activation energies of predicted compounds from AIMD simulations and experiment.<sup>a</sup>He et al.<sup>34</sup><sup>b</sup>Ong et al.<sup>62</sup><sup>c</sup>Kamaya et al.<sup>1</sup><sup>d</sup>Kato et al.<sup>2</sup> (values refer to  $\text{LiSiPSCl}$  composition).<sup>e</sup>Bron et al.<sup>82</sup>

hypothetical oxide compounds  $\text{Li}_{10}\text{MP}_2\text{O}_{12}$  ( $\text{M} = \text{Si}, \text{Ge}, \text{Sn}$ ) with the LGPS structure were calculated to have high  $E_{\text{hull}}$  of greater than 70 meV/atom (Figure 5B), indicating highly exothermic decomposition reactions to their thermodynamic phase equilibria, including  $\text{Li}_3\text{PO}_4$  and  $\text{Li}_4\text{MO}_4$  ( $\text{M} = \text{Si}, \text{Ge}$ ).<sup>62</sup>

AIMD simulations predicted that  $\text{Li}_{10}\text{SiP}_2\text{S}_{12}$  and  $\text{Li}_{10}\text{SnP}_2\text{S}_{12}$  have fast  $\text{Li}^+$  diffusion at RT (Figure 5C).  $\text{Li}_{10}\text{SnP}_2\text{S}_{12}$  was predicted by AIMD simulations to have a high  $\text{Li}^+$  ionic conductivity of  $6 \text{ mS cm}^{-1}$  at 300 K and an activation energy of 0.24 eV (Figure 5D).<sup>62</sup> Synthesized  $\text{Li}_{10}\text{SnP}_2\text{S}_{12}$  was reported to have a bulk  $\text{Li}^+$  conductivity of  $7 \text{ mS cm}^{-1}$  at 300 K and an activation energy of 0.27 eV, which showed excellent quantitative agreement with AIMD simulation results.<sup>82</sup> AIMD simulations also predicted  $\text{Li}_{10}\text{SiP}_2\text{S}_{12}$  to have a high ionic conductivity of  $23 \text{ mS cm}^{-1}$  at 300 K and a low activation energy of 0.20 eV.<sup>62</sup> Kuhn et al.<sup>83</sup> successfully synthesized  $\text{Li}_{10}\text{SnP}_2\text{S}_{12}$  and  $\text{Li}_{11}\text{Si}_2\text{PS}_{12}$  and measured  $\text{Li}^+$  diffusivities and activation energies in these materials similar to that of LGPS, consistent with the trend observed from AIMD simulations.<sup>62</sup> The experiments by Kato et al. reported slightly slower diffusion in  $\text{Li}_{10}\text{SiP}_2\text{S}_{12}$  than in  $\text{Li}_{10}\text{GeP}_2\text{S}_{12}$ .<sup>85</sup> It should be noted that quantitative comparison may be difficult given the high level of statistical uncertainty from AIMD simulation results<sup>39</sup> and potential variance from experiments (Section 2.1).<sup>79,80</sup> Krauskopf et al. recently proposed a complex interplay between lattice softness, local atomic bonding, and bottleneck size to explain the lower conductivity exhibited by  $\text{Li}_{10}\text{SnP}_2\text{S}_{12}$ .<sup>86</sup> Kato et al. synthesized  $\text{Li}_{9.54}\text{Si}_{1.74}\text{P}_{1.44}\text{S}_{11.7}\text{Cl}_{0.3}$  ( $\text{LiSiPSCl}$ ), a doped variant of  $\text{Li}_{10}\text{SiP}_2\text{S}_{12}$ , with a measured ionic conductivity of  $25 \text{ mS cm}^{-1}$ ,<sup>2</sup> which is close to the calculated  $\text{Li}^+$  conductivity of  $23 \text{ mS cm}^{-1}$  in  $\text{Li}_{10}\text{SiP}_2\text{S}_{12}$ .<sup>62</sup> The successful computational design of  $\text{Li}_{10}\text{SiP}_2\text{S}_{12}$  and  $\text{Li}_{10}\text{SnP}_2\text{S}_{12}$  demonstrates the capability of first-principles computation in accurately predicting new SE materials and their ion-conducting properties.

As illustrated by this computational prediction of new SEs based on the LGPS structure, a scheme of designing new SE materials using first-principles computation (Figure 5) can be outlined as follows:

- 1) Generate candidate materials by substituting or doping a known structure or from structure prediction algorithms.
- 2) Evaluate the phase stability of the candidate materials, which may be quantified using a calculated metric such as energy above hull  $E_{\text{hull}}$ . The materials predicted with poor phase stability are excluded, and only those with reasonable phase stability are further studied.
- 3) Calculate the properties of the candidate materials. For SE materials, diffusional properties, such as ionic conductivity and activation energy, can be accurately predicted by AIMD simulations (Figure 5D). In addition, other properties of SEs desirable for ASBs, for example, electrochemical stability (Section 4), interface compatibility (Section 5), and electronic conduction,<sup>87</sup> can also be evaluated by first-principles computation.

This computational workflow has been successfully applied for designing novel  $\text{Li}^+$ ,  $\text{Na}^+$ ,<sup>59,76</sup>  $\text{Mg}^{2+}$ ,<sup>88</sup>  $\text{O}^{2-}$ ,<sup>33</sup> and  $\text{H}^{-35}$  ion conductors. Using this computational approach, one can predict dopants that increase the ionic conductivity of materials. For example, the computation study by Ong and co-workers predicted the substitution of S with Cl would significantly increase the  $\text{Na}^+$  conductivity of  $\text{Na}_3\text{PS}_4$ , and the predicted doped compositions were verified in experiments.<sup>89,90</sup> The importance of confirming the phase stability of computationally predicted materials should be emphasized. All known SICs, such as LGPS and LLZO, and successfully predicted SICs, such as  $\text{Li}_{10}\text{SnP}_2\text{S}_{12}$ ,  $\text{Li}_{10}\text{SiP}_2\text{S}_{12}$ , and  $\text{LiZnPS}_4$ , have a small  $E_{\text{hull}}$  of less than 20 meV/atom. The doped compositions should also have good phase stability, otherwise they may be difficult to synthesize in experiments.

While many current studies focus on doping or substitution of known materials for better performance, exploring novel crystal structural frameworks is of great potential for the discovery of new SE materials. New candidate structures have been uncovered by computational approaches such as structure screening using the bond valence method,<sup>91,92</sup> machine-learning algorithms,<sup>93</sup> structure prediction algorithms,<sup>94</sup> and structural substitution algorithms.<sup>95,96</sup> As motivated by the spirit of MGI,<sup>21</sup> this computational workflow can be scaled up to rapidly screen a large number of possible materials for the most promising high-performance candidate. High-throughput computational screening can rapidly reject many candidate compounds with poor stability or undesirable properties and significantly narrow the scope of candidate materials. As a result, the most promising candidate materials can be prioritized in laboratory experiments. Compared with conventional trial-and-error materials development, this scheme of computational materials design represents an exciting opportunity for accelerating the discovery of new materials.

#### 4. Electrochemical Stability of Solid Electrolytes

There was a widespread perception that SEs had superior electrochemical stability compared with conventional liquid or polymer electrolytes. This perception was based on the reported electrochemical window of 0–5 V from cyclic voltammetry (CV) measurements using semi-blocking electrodes for a number of SEs.<sup>1,64,97,98</sup> In contrast, thermodynamic calculations based on DFT energies revealed that the thermodynamic intrinsic electrochemical windows of these SEs are significantly narrower than the 0–5 V window (Section 4.2).<sup>38,63,64,71</sup> The understanding of this discrepancy between the thermodynamic intrinsic electrochemical window of SEs

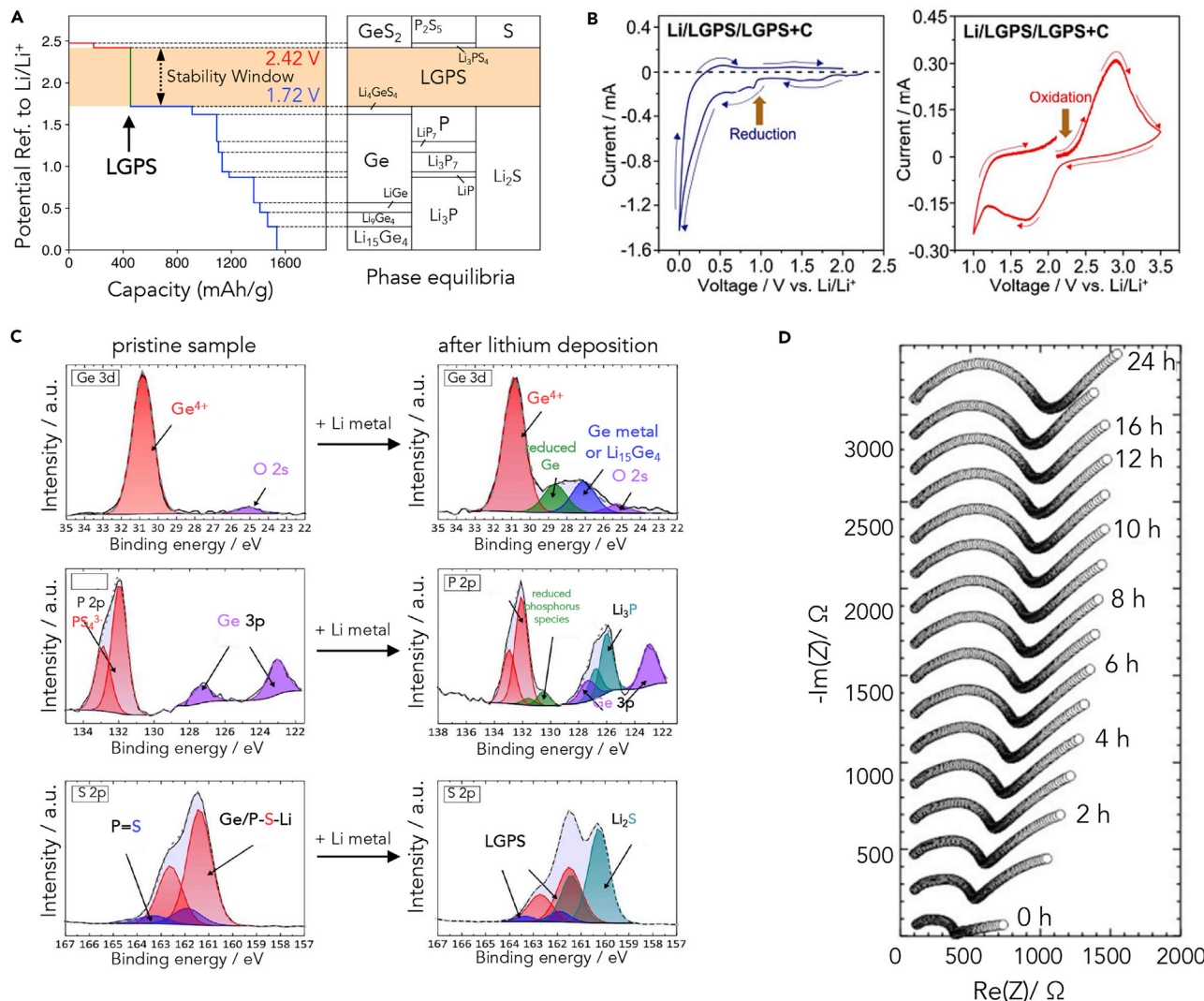


**Figure 6. Electrochemical Stability of LGPS Solid Electrolyte**

(A) Calculated equilibrium voltage profile (left) and phase equilibria (right) of LGPS. The different values from previous studies<sup>63,64,70,101</sup> are caused by a newly added energy correction on elementary S in the MP. Adapted from Han et al.<sup>64</sup> with permission. Copyright 2016, Wiley-VCH.

(B) Cyclic voltammetry curves of the Li-LGPS-LGPS-C-Pt cell, indicating the reduction and oxidation peaks in the anodic and cathodic scans, respectively. Reproduced from Han et al.<sup>64</sup> with permission. Copyright 2016, Wiley-VCH.

(C) XPS spectra of Ge, P, and S for pristine LGPS and after deposition of the Li metal layer.

(D) Impedance spectra showing the increase in resistance of the Li-LGPS-Li cell over time. Reproduced from Wenzel et al.<sup>100</sup> with permission. Copyright 2016, American Chemical Society.

and conventional CV measurements using semi-blocking electrodes are reviewed in Sections 4.1 and 4.2. The general trends of the electrochemical stability and the design principles to improve the electrochemical stability of SEs are reviewed in Section 4.3. The effects of formed interphase layers, which play a crucial role in stabilizing the SE, are reviewed in Section 5.

#### 4.1. Evaluating Electrochemical Stability of Solid Electrolytes

The lithiation and delithiation reactions of SE materials as a function of potential can be obtained from thermodynamic calculations using the materials database (Section 2.2.2). Figure 6A shows the calculated thermodynamic equilibrium voltage plateaus for all lithiation and delithiation reactions for LGPS.<sup>64</sup> The first lithiation plateau

occurs at 1.7 V with  $P^{5+}$  reduction, and further lithiation reactions are followed by  $Ge^{4+}$  reduction, lithiation of phosphorus, and Li-Ge alloying reactions. The phase equilibria of LGPS at 0 V (or in contact with Li metal) are  $Li_2S$ ,  $Li_3P$ , and  $Li_{15}Ge_4$  (Figure 6A). The first delithiation plateau at approximately 2.4 V corresponds to  $S^{2-}$  oxidation reactions, similar to the reactions in Li-S batteries.<sup>99</sup> Therefore, the thermodynamic intrinsic electrochemical window of LGPS is only 1.7–2.4 V, in contrast to the wide 0–5 V window measured using semi-blocking CV.<sup>1</sup> The reduction of  $Ge^{4+}$  and  $P^{5+}$  at low potential and the oxidation of  $S^{2-}$  at high potential have been confirmed by multiple *in situ* and *ex situ* X-ray photoelectron spectroscopy (XPS) studies (Figure 6C).<sup>64,98,100</sup>

This discrepancy between computation and experimental CV measurements of electrochemical windows of SEs can be explained by the limitations of the conventional semi-blocking electrode setup for CV measurements in all-solid-state cells and by previous oversight of formed interphase layers between SE and electrodes. As proposed by Han et al., in conventional CV measurements, the small surface area between the SE and the semi-blocking electrodes limits the kinetics of the decomposition reactions and the measurable redox current.<sup>98</sup> In fact, a small decomposition current was observed from CV measurements of a Li-LGPS-Pt cell using semi-blocking electrodes.<sup>64</sup> If this small redox current were overlooked, the stability windows of SEs would be overestimated. In addition, the decomposition reactions of SE can form an interphase layer between the SE and electrodes. The growth of an interphase layer between LGPS and Li metal was observed by *in situ* XPS and time-resolved impedance spectroscopy experiments (Figures 6C and 6D).<sup>100,102</sup> As reviewed in Section 5, the formed interphase layer, depending on its properties, may kinetically stabilize the SE and inhibit further decomposition.<sup>63,103</sup> To summarize, CV measurements using the semi-blocking electrode setup overestimate the true electrochemical window governed by the intrinsic thermodynamics of SEs. The reported wide electrochemical windows of SEs are largely an artifact of the semi-blocking electrode setup. Since the intrinsic thermodynamics of SEs govern interphase formation and degradation (Section 5), proper evaluation of the true electrochemical window of SEs is critical for the interface engineering in ASBs.

To resolve this problem, Han et al. proposed a Li-LGPS-LGPS-C-Pt cell, in which the LGPS-C electrode was a composite formed by mixing a significant fraction of graphite (e.g., 25 wt % in Han et al.<sup>64</sup>) into LGPS.<sup>64</sup> The incorporation of this electronically conducting carbon served to enhance electron transport and increase the physical contact area for charge-transfer reactions, thereby improving the decomposition reaction kinetics.<sup>104</sup> Using this technique, the reduction of LGPS was observed to start at 1.6 V, and the oxidation of LGPS was observed at 2.7 V (Figure 6B).<sup>64,98</sup> These reactions were confirmed to be  $Ge^{4+}$  reduction and  $S^{2-}$  oxidation by XPS spectra.<sup>64,98</sup> Therefore, the electrochemical window measurements performed using these mixed composite electrodes agree well with the calculated intrinsic thermodynamic window of the material. Compared with semi-blocking electrodes, this composite electrode setup can better represent the electrodes in bulk ASBs, in which the SE is mixed with the active electrode material and electronically conducting additives.<sup>1,2,105,106</sup>

The thermodynamic intrinsic stability window of the SEs and their decomposition products are critical for the performance of ASBs. When the cycling voltage is beyond the thermodynamic intrinsic stability window of an SE, the electrochemical reactions of SEs lead to capacity fade and low Coulombic efficiency in the first and

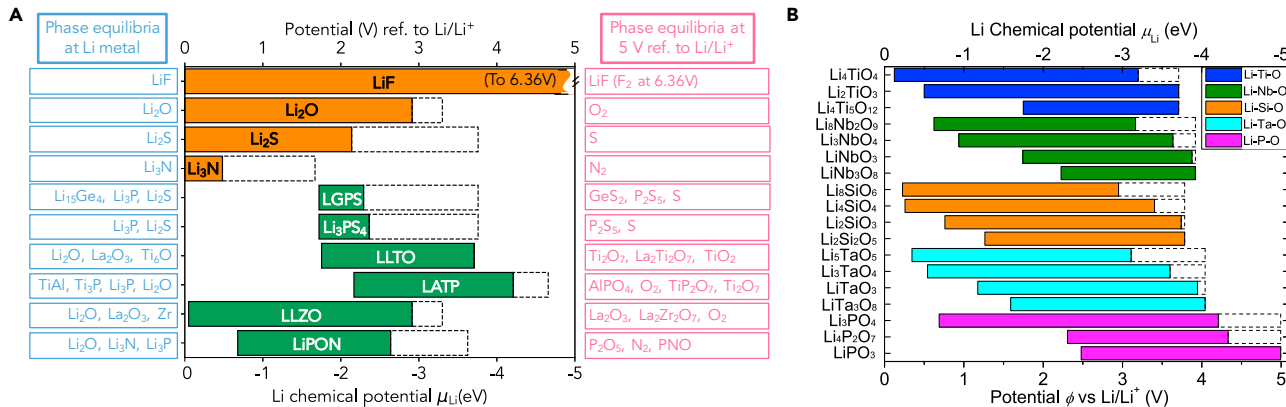


**Figure 7. Thermodynamic Intrinsic Electrochemical Stability Windows**

(A) Li binary compounds (orange), selected solid electrolytes (green), and corresponding phase equilibria of the solid electrolytes at 0 V and 5 V. The dashed boxes mark the potential at which the compound is fully delithiated.

(B) Selected Li ternary compounds, color-coded by compositional group and organized by Li content. Reproduced from Zhu et al.<sup>70</sup> with permission. Copyright 2016, Royal Society of Chemistry.

subsequent cycles. The redox behavior of some SEs may exhibit a significant amount of partially reversible capacity, partially converting these SEs into electrodes as observed in LGPS.<sup>98</sup> The reaction products can form at the interfaces within the composite ASB electrode and greatly affect the interfacial resistance (Figure 6D).<sup>100–103</sup> The issue of interfacial compatibility and its effect on ASB performance are further discussed in Section 5.

#### 4.2. Intrinsic Electrochemical Window of Solid Electrolytes

As found using thermodynamic calculations, most known SE materials have a thermodynamic intrinsic electrochemical window significantly narrower than 0–5 V (Figure 7). Like LGPS, other sulfide SEs, such as Li<sub>3</sub>PS<sub>4</sub>, Li<sub>7</sub>PS<sub>11</sub>, and argyrodite Li<sub>6</sub>PS<sub>5</sub>Cl, show similarly narrow thermodynamic electrochemical windows, undergoing reduction at 1.7 V and oxidation at 2.4 V (Figure 7), and exhibit similar reduction of P<sup>5+</sup> cations and oxidation of S<sup>2-</sup> at low and high potentials, respectively.<sup>63,71</sup> The reduction of sulfide SEs in the presence of Li metal<sup>100,107,108</sup> and the oxidation of sulfide SEs<sup>109–111</sup> were confirmed in multiple experimental studies.

Oxide-based SEs generally have a wider electrochemical stability window than sulfides, as indicated by thermodynamic calculations (Figure 7). The oxidation potential of common oxide SEs ranges between 2.9 and 4.3 V, which is significantly higher than that of sulfide SEs.<sup>63,71</sup> These potentials correspond to O<sup>2-</sup> oxidation, leading to O<sub>2</sub> release from oxides. Oxygen redox and oxygen loss at high voltages are known issues in oxide cathode materials.<sup>112,113</sup> Many SEs have equilibrium oxidation potentials higher than the equilibrium potentials of oxygen evolution reactions of Li<sub>2</sub>O and Li<sub>2</sub>O<sub>2</sub> in Li-O<sub>2</sub> batteries.<sup>114</sup> However, given the kinetic limitations in oxygen evolution reactions,<sup>114,115</sup> the oxidation reactions, especially at the solid interfaces in ASBs, may occur at potentials significantly higher than the thermodynamic oxidation potential. These kinetic limitations may explain the oxidation potential higher than 5 V observed in experiments for oxide SEs.<sup>64,97,116</sup> The different oxidation reactions of oxides and sulfides explain the differences in their anodic limits.

The reduction of SEs is largely determined by the reduction of cations within the SE. For example, from thermodynamic calculations, LATP and LLTO exhibit the

reduction of  $Ti^{4+}$  at 2.2 V and 1.8 V,<sup>63,71</sup> respectively, consistent with CV measurements and XPS characterizations.<sup>117–120</sup> All phosphate and thio-phosphate SEs show the reduction of  $P^{5+}$  at low potentials. The reduction of phosphorus in LiPON was reported in computation studies<sup>63,71</sup> (Figure 7A) and *in situ* XPS experiments (Section 5.1),<sup>121</sup> although LiPON has been demonstrated to be Li metal compatible.<sup>4,122–124</sup> This Li-LiPON compatibility can be explained by the formed  $Li^+$  conducting and  $e^-$  insulating interphase layers (Section 5). Among oxide SEs, LLZO shows the lowest thermodynamic reduction potential against Li, close to 0 V.<sup>63,71</sup> This calculation substantiates experimental reports of the stability of garnet LLZO against Li metal and of Li metal electrodes enabled by LLZO SE.<sup>3,125</sup> The Li-rich anti-perovskite  $Li_3OCl$ , which has a mixed anion chemistry and does not contain metal cations, is thermodynamically stable against Li metal, confirming its observed compatibility with Li metal electrodes.<sup>126</sup>

#### 4.3. General Trends in the Electrochemical Stability of Solid Electrolytes

Materials with different cations, anions, and Li content exhibit different electrochemical stabilities. The anodic limits of lithium binary compounds show a clear trend with respect to the anion chemistry (Figure 7A). Lithium fluoride, LiF, has the highest oxidation potential, followed by  $Li_2O$  and then  $Li_2S$ , and lithium nitride,  $Li_3N$ , has the lowest oxidation potential among these four binary compounds. These stability trends with respect to anion chemistry also hold for ternary systems, as shown by the computation over a wide range of compositions (Figure 8). The oxidation potential is heavily dependent on anion chemistry and Li content (Figure 8B). Increasing the Li content in the composition with the same anion and cation lowers the oxidation potential (Figure 7B). Based on these stability trends, fluorides or oxides with low Li content in general exhibit high oxidation potentials.

The cathodic limit shows clear trends with respect to anion, cation, and Li content of the material. While Li binary compounds are stable against Li metal (Figure 7A), thermodynamic calculations by Zhu et al. showed that most Li ternary sulfides, oxides, and halides are reduced at low potentials and are not stable against Li metal (Figure 8A).<sup>101</sup> The reduction reaction at low potential is a result of the reduction of the non-Li cation during lithiation. Among all anion chemistries, nitrides exhibit the lowest cathodic limits in comparison with oxides, sulfides, or fluorides. Most importantly, many nitride compounds are thermodynamically stable against Li metal (Figure 8A).<sup>101</sup> These Li binary compounds and Li metal nitrides with thermodynamic intrinsic stability against Li metal can be used to protect electrolyte from the strong reduction of Li metal. In addition, the formation of passivation interphase layers of these Li stable materials can also provide stability at the interface and extend the observed electrochemical stability window of SE (Section 5).

These thermodynamic trends from computation can guide the selection and design of materials with desirable electrochemical windows. Fluoride-based compounds with low Li content would have high anodic limits, and nitride-based materials with high Li content would have low cathodic limits. Therefore, the materials chemistries for high anodic limits contradict those for low cathodic limits. It would be challenging to develop a single SE material with a thermodynamic intrinsic electrochemical window of 0–5 V. As shown in Section 5, the stability of many SEs can be significantly improved by the formation of interphase layers, similar to the formation of solid electrolyte interphase (SEI) layers that stabilize the liquid electrolyte in commercial Li-ion batteries. Formed interphase layers extend the observed electrochemical stability of SEs beyond the thermodynamic intrinsic stability window.<sup>63,71</sup>

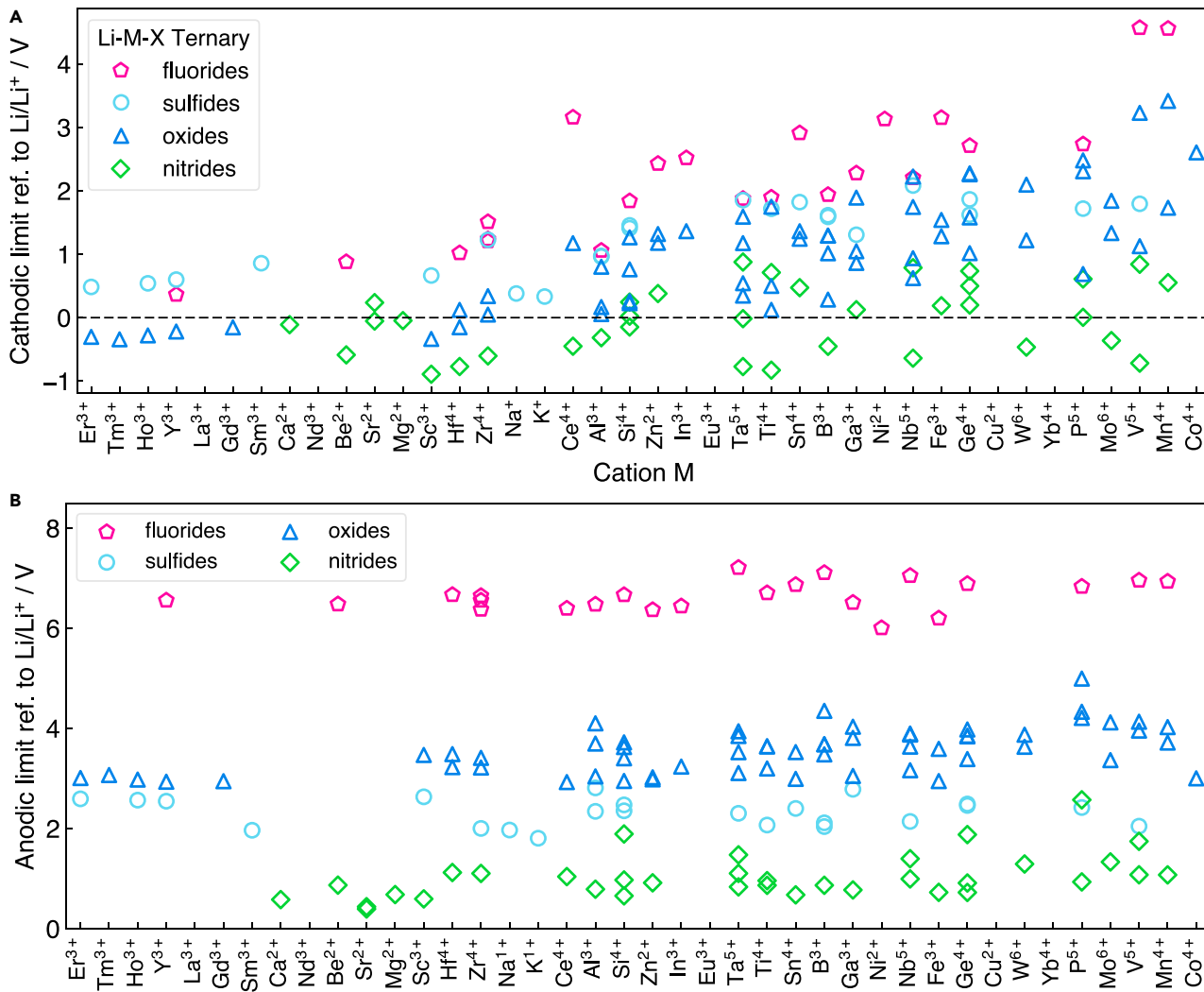


**Figure 8. Stability Trends in Li-M-X Ternary Compounds (M = cation, X = N, O, S, or F)**

(A) Cathodic limit. Only cations M at their highest common valence state were considered. Dashed line refers to the potential of  $\text{Li}/\text{Li}^+$ .  
 (B) Anodic limit. Reproduced with permission from Zhu et al.<sup>101</sup> Copyright 2017, Wiley-VCH.

## 5. Interface Stability and Compatibility in All-Solid-State Batteries

Due to the limited stability of SEs, exothermic reactions occur at the interfaces between SEs and electrodes, as reported by computational and experimental studies.<sup>2,6,64,100,121,127</sup> These interfacial reactions in many cases are detrimental for ASB performance, leading to low Coulombic efficiency, high interfacial resistance, and mechanical failure at the SE-electrode contact during electrochemical cycling.<sup>98,128</sup> Three main mechanisms contribute to interfacial reactions and the formation of interphase layers: (1) the electrochemical decomposition of the SE itself under applied cycling voltage; (2) chemical reactions between the SE and the electrode (or other mixtures, such as electronically conducting carbon, interfacial coatings, or binders); (3) electrochemical reactions between the SE and the electrode (or mixtures) under the cycling voltage of the battery. The electrochemical reactions of the SE in (1) and of the interfaces in (3) are a result of the cycling battery voltage. The chemical reactions of the interfaces in (2) may occur during the assembly of ASBs, when the two materials are placed into physical contact, and during

high-temperature sintering, which may be performed to improve interfacial contact and to reduce the porosity of SE-electrode composite.<sup>129–131</sup> Since these solid-solid interfaces buried within the ASBs are difficult to directly access in experiments, computational studies provide valuable insight into the interface stability in ASBs.

### 5.1. Li Metal-Solid Electrolyte Interface

As reviewed in [Section 4](#), computational and experimental studies demonstrate the lack of thermodynamic intrinsic stability of most SEs against Li metal. When SEs are in contact with Li metal, exothermic lithiation and reduction reactions happen spontaneously and lead to the formation of interphase layers. The conducting properties of the interphase layers formed are a crucial factor in determining the interfacial compatibility of SEs and Li metal anode.

For example, the use of LiPON was demonstrated in a Li metal thin-film solid-state battery with a long cycle life of over 10,000 cycles.<sup>4,122–124</sup> However, thermodynamic calculations ([Section 4.2](#)) showed that the Li reduction of LiPON is thermodynamically favorable with the phase equilibria consisting of Li<sub>3</sub>N, Li<sub>3</sub>P, and Li<sub>2</sub>O at the Li metal interface.<sup>63</sup> The formation of these reaction products at the LiPON-Li metal interface was confirmed by *in situ* XPS studies ([Figure 9A](#)).<sup>121</sup> This interphase layer is ionically conducting but electronically insulating, and thereby passivates the Li-LiPON interface. In addition, the Li-ion conductors Li<sub>3</sub>N and Li<sub>3</sub>P facilitate ion transport, leading to low interfacial resistance. Therefore, the compatibility observed between LiPON and Li metal is a result of the formation of a passivating interphase layer, similar to the SEI formed between graphite anode and liquid electrolyte in commercial Li-ion batteries.

Unlike LiPON, other SEs do not form passivating layers upon contact with Li metal. For example, LGPS forms mixed ionic and electronic conducting (MIEC) interphase layers consisting of Li<sub>2</sub>S, Li<sub>3</sub>P, and Li<sub>15</sub>Ge<sub>4</sub>, in contact with Li metal ([Section 4](#)). This interphase layer is MIEC due to the electronically conductive Li-Ge alloy. This MIEC interphase layer permits the transport of both Li<sup>+</sup> and e<sup>-</sup> from the Li metal anode into the bulk SE and allows the favorable decomposition of the SE to continue, leading to a rapid thickening of the interphase layer and an increase of interfacial resistance as observed in time-resolved impedance measurements ([Figure 6D](#)).<sup>120</sup> Similarly, the reduction of LLTO and LATP SEs in contact with Li metal also leads to the formation of MIEC interphase layers.<sup>117–120</sup> The ionic and electronic conducting properties of the spontaneously formed interphases are crucial for the interfacial compatibility in ASBs.

### 5.2. Solid Electrolyte-Cathode Interface

Interphase formation at the SE-cathode interface was predicted in computation and was observed in experiments. The chemical reactions of SE and cathode are thermodynamically favorable to form other phases (e.g., phase equilibria) with lower energies, according to the thermodynamic calculations described in [Section 2.2.3](#). For example, a possible reaction of LPS and LiCoO<sub>2</sub> (LCO) to form a combination of the phases Co<sub>9</sub>S<sub>8</sub>, Li<sub>2</sub>S, Li<sub>2</sub>SO<sub>4</sub>, and Li<sub>3</sub>PO<sub>4</sub> has an exothermic reaction enthalpy  $\Delta H_D$  of –0.41 eV/atom ([Figure 9C](#)).<sup>70</sup> The reaction is driven by the favorable tendency of the Co cation in LCO to form cobalt sulfides and also by the preference of the P<sup>5+</sup> and S<sup>2-</sup> in LPS to form phosphate and sulfate, respectively. In agreement with these computational results, experiments reported the formation of phosphates at the interface between a Li<sub>2</sub>S-P<sub>2</sub>S<sub>5</sub> glass-ceramic SE and a layered cathode.<sup>132</sup> Energy-dispersive X-ray spectroscopy (EDX) analyses of the interfacial layer between LCO and Li<sub>2</sub>S-P<sub>2</sub>S<sub>5</sub> by Sakuda et al. ([Figure 9B](#)) indicated cobalt sulfides in

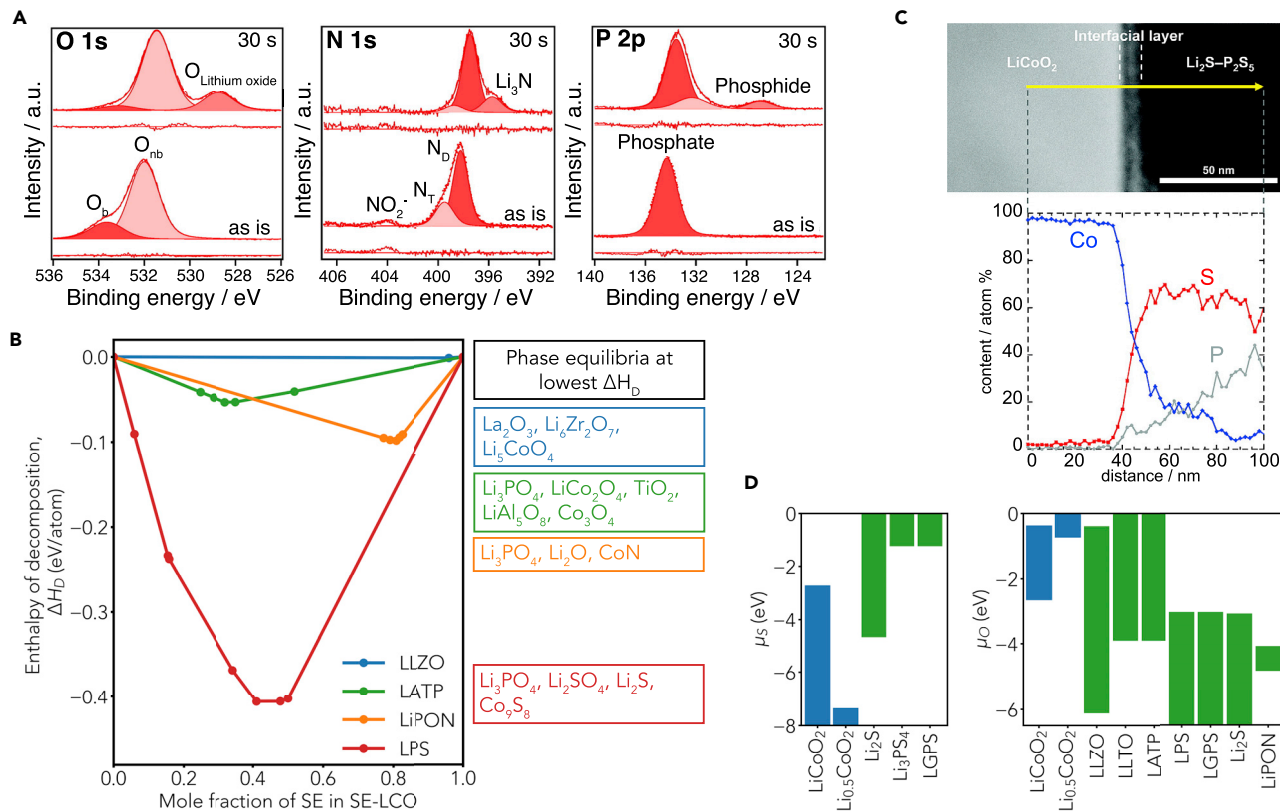


**Figure 9. Stability and Interphase Formation at the Solid Electrolyte-Electrode Interface**

(A) XPS spectra of the O 1s, N 1s, and P 2p in LiPON before and after exposure to Li metal. Reproduced from Schwöbel et al.<sup>121</sup> with permission. Copyright 2015, Elsevier.

(B) Calculated enthalpy of decomposition of LCO-LPS as a function of the mixing ratio of LPS SE and phase equilibria (in box) with largest magnitude of decomposition enthalpy.

(C) High-angle annular dark-field-scanning transmission electron microscopy image of the cross-section of the LCO-Li<sub>2</sub>S-P<sub>2</sub>S<sub>5</sub> interface and corresponding EDX profiles for Co, P, and S. Reproduced from Sakuda et al.<sup>6</sup> with permission. Copyright 2010, American Chemical Society.

(D) Calculated  $\mu_O$  and  $\mu_S$  stability window of LCO cathode and SEs. Reproduced from Zhu et al.<sup>70</sup> with permission. Copyright 2016, Royal Society of Chemistry.

the interfacial layer.<sup>6</sup> Cobalt sulfides are electronically conductive,<sup>133</sup> and thereby form an MIEC interphase layer, leading to significant interfacial degradation and poorer Li-ion transport across the interface.

In addition, the chemical reactions between SEs and cathodes are different for charged and discharged states of cathodes or at different applied voltages. Under high applied voltage, the reaction between an SE and a cathode may become more favorable and form different phase combinations. For many SEs with low anodic limits, thermodynamic calculations suggest the interfacial decomposition reaction is more favorable when the battery is charged or is under high voltage.<sup>70</sup> For example, Li<sub>3</sub>PS<sub>4</sub> reacts much more favorably with Li<sub>0.5</sub>CoO<sub>2</sub> ( $\Delta H_D = -0.56$  eV/atom) or at 5 V ( $\Delta H_D = -1.27$  eV/atom) than with LCO ( $\Delta H_D = -0.41$  eV/atom). The reactions for delithiated cathodes at high voltage are more favorable because lower Li chemical potential drives the delithiation and oxidation of SEs. Experimental studies confirm the redox behavior of these sulfide SEs and their electrode composites at different voltages during electrochemical cycling.<sup>107,109–111</sup> In contrast, the SEs with high anodic limits, such as oxide SEs LLTO and LATP, are stable with Li<sub>0.5</sub>CoO<sub>2</sub> but not with LCO. Due to the dependence of stability on the state of charge and

applied potential, interface compatibility must be satisfied over the operating voltage range of the ASB.

In general, sulfide SEs have poor stability and compatibility with oxide cathodes. The exothermic reactions of thio-phosphate sulfide SEs with oxide cathodes, including LCO, LiFePO<sub>4</sub>, LiMnO<sub>2</sub>, and LiNiO<sub>2</sub>, were reported from thermodynamic calculations<sup>70,71</sup> and in experiments.<sup>110,111</sup> The computation-predicted phase equilibria indicate these decomposition reactions tend to form transition metal sulfides. From thermodynamic calculations, the chemical potential of sulfur,  $\mu_S$ , in the sulfide SEs exhibits less negative values than those in the oxide cathodes (Figure 9D).<sup>70</sup> Because the stability ranges of  $\mu_S$  for these materials do not overlap, the sulfide SEs and oxide cathodes cannot simultaneously satisfy the equilibrium condition of equal chemical potential. The same analyses of the chemical potential of oxygen,  $\mu_O$ , show that sulfide SEs and oxide cathodes cannot have equal  $\mu_O$  and therefore cannot reach a thermodynamic equilibrium. Therefore, different anion chemistries cause the incompatibility of thio-phosphate sulfide SEs and common oxide cathodes. As a result of this incompatibility, reactions occur with O and S exchange between the SE and cathode materials. Experiments reported the formation of phosphates at the Li<sub>2</sub>S-P<sub>2</sub>S<sub>5</sub> glass-ceramic SE, and layered cathode interface,<sup>132</sup> and the formation of elementary sulfur, polysulfides, P<sub>2</sub>S<sub>x</sub> species ( $x > 5$ ), and LiCl at the Li<sub>6</sub>PS<sub>5</sub>Cl and oxide cathode interface.<sup>111</sup>

In contrast, SE and cathode materials with the same anion chemistry generally exhibit better stability with each other. Sulfide SEs are more compatible with sulfide cathodes such as Li<sub>2</sub>S, LiTiS<sub>2</sub>, and LiVS<sub>2</sub> than with oxide cathodes, as shown in thermodynamic calculations.<sup>71</sup> Multiple experimental studies indeed report good cyclability and reversible capacity of thio-phosphate SEs with sulfur and sulfide (e.g., LiTiS<sub>2</sub>) cathodes.<sup>134–136</sup> Oxide SEs are in general more stable with oxide cathodes than with sulfide SEs, as shown by less exothermic reaction energies.<sup>70,71</sup> Nonetheless, the interfacial chemical reactions between oxide SEs and oxide cathodes are still thermodynamically favorable. The formation of interphase layers between oxide SEs and oxide cathodes is often observed after high-temperature heat treatment at several hundred degrees Celsius, which is often performed to improve the solid-solid interfacial contact.<sup>129–131</sup> A combined computational and experimental study by Miara et al. also observed the formation of transition metal oxides, such as Mn<sub>2</sub>O<sub>3</sub>, TiO<sub>2</sub>, and Co<sub>3</sub>O<sub>4</sub>, along with AlPO<sub>4</sub> and Li<sub>3</sub>PO<sub>4</sub> at the interface of LATP and the high-voltage spinel cathodes, such as Li<sub>2</sub>NiMn<sub>3</sub>O<sub>8</sub>, Li<sub>2</sub>FeMn<sub>3</sub>O<sub>8</sub>, and LiCoMnO<sub>4</sub>, after heat treatment.<sup>129</sup> This study also reported that the heat treatment of Ta-doped LLZO garnet SE and these spinel cathodes led to the formation of the insulating phases La<sub>2</sub>Zr<sub>2</sub>O<sub>7</sub>, La<sub>2</sub>O<sub>3</sub>, La<sub>3</sub>TaO<sub>7</sub>, and LaMnO<sub>3</sub>. The formed interphase layers between oxide SEs and oxide cathodes can be thin and passivating, but the interfacial resistance would be high if the formed interphase layers have poor Li<sup>+</sup> conductivity.<sup>70,129</sup>

A well-known example of a compatible SE-cathode interface is between LiPON and oxide cathodes, such as LCO and LiNi<sub>0.5</sub>Mn<sub>1.5</sub>O<sub>4</sub> (LNMO).<sup>4,122–124</sup> ASBs constructed using these materials form stable interfaces, displaying good capacity retention and long cycle life. However, thermodynamic calculations also suggest that LiPON exothermically reacts with LCO,<sup>70</sup> and the reaction between LiPON and LCO has been observed by *in situ* scanning transmission electron microscopy-electron energy loss spectroscopy and XPS experiments, where interphase products including Co<sub>3</sub>O<sub>4</sub>, Li<sub>2</sub>O, Li<sub>2</sub>O<sub>2</sub>, Li<sub>3</sub>PO<sub>4</sub>, and LiNO<sub>2</sub> were observed in different characterization studies.<sup>137–139</sup> Therefore, the LiPON-cathode compatibility also originates from

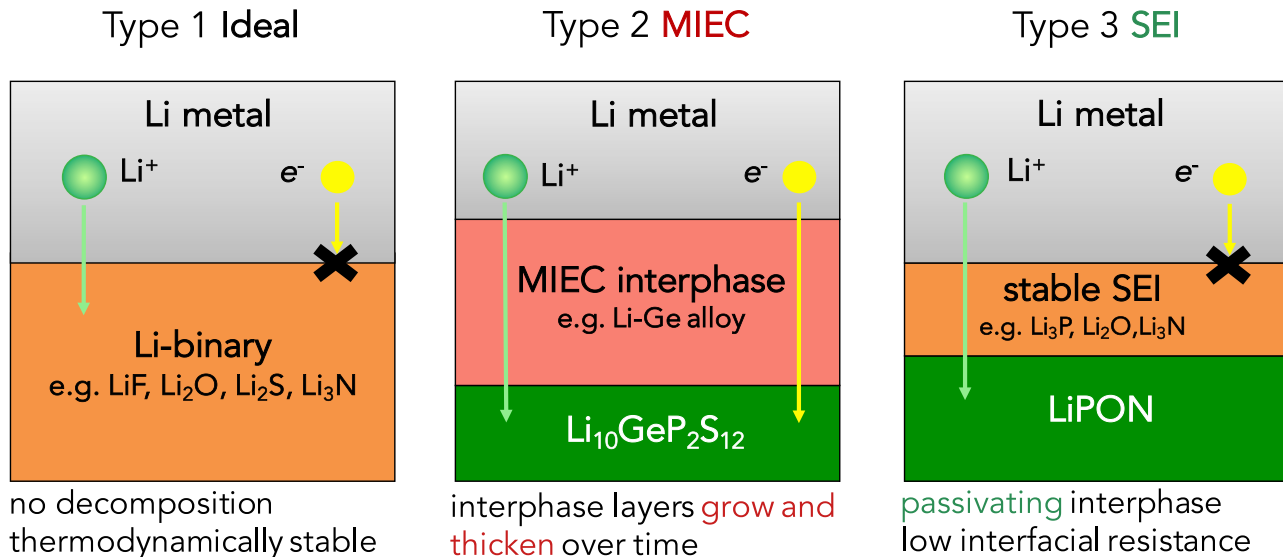


**Figure 10. Illustration of Different Types of Li Metal-SE Interfaces**

the formed interphase layer, which passivates the interface and prevents further reaction, similar to the Li-LiPON interface.

### 5.3. The Classification of Interface Types

As reviewed in Sections 5.1 and 5.2, computational and experimental studies indicate that many SEs are not thermodynamically stable against Li metal anode and common oxide cathodes. Instead, the interface compatibility between SE and electrodes originates from the passivation effect determined by the ionic and electronic transport properties of the spontaneously formed interphase layer. The SE-electrode interfaces can be categorized into three types based on their stability and conducting properties (Figure 10):<sup>63,70,120</sup>

- 1) Type 1 interface: the two materials in contact are intrinsically stable with each other, i.e., these two materials are in thermodynamic equilibrium with one another and do not exothermically react. For example, Li metal forms type 1 stable interfaces with Li binary compounds such as LiF, Li<sub>2</sub>O, Li<sub>2</sub>S, and Li<sub>3</sub>N, but not with most SEs. Type 1 interfaces are rare among SEs with commonly used cathodes.
- 2) Type 2 interface: the two materials in contact form an MIEC interphase layer, which cannot passivate the SE. The interphase layer formed can transport both Li<sup>+</sup> and e<sup>-</sup> leading to continuous decomposition. The growth rate of interphase thickness and the resulting interfacial resistance depend on the ionic and electronic conductivities of the interphase layer formed. Thus, type 2 interfaces with high electronic and ionic conductivities may cause a rapid short circuit in the cell, while interfaces with low electronic conductivity may exhibit slow, parasitic degradation spanning the lifetime of the ASB.<sup>140</sup> Many SE materials, such as LLTO, LATP, and LGPS, form type 2 interfaces in contact with Li metal, because MIEC metallic phases form from the reduction of metal cations. Similarly, sulfide SE-oxide cathode interfaces are also type 2 due to the formation of electronically conducting transition metal sulfides. Type 2 interfaces should be avoided in ASBs.
- 3) Type 3 interface: the two contacting materials with an interphase layer that is electronically insulating and ionically conducting, similar to the SEI in liquid

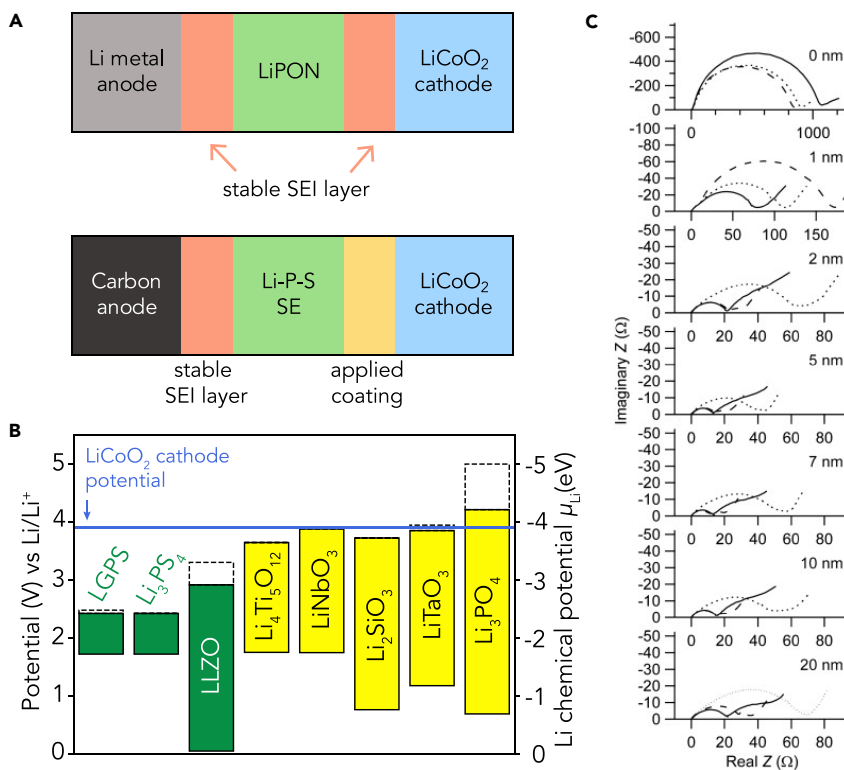


**Figure 11. Interface Engineering in ASBs**

(A) Schematic illustration of Li-LiPON-LCO thin-film cell and graphite-Li-P-S-SE-coated-LCO bulk-type cell as successful ASB examples.

(B) Electrochemical window of common cathode coating materials (yellow) compared with selected SE materials (green). Reproduced from Zhu et al.<sup>63</sup> with permission. Copyright 2015, American Chemical Society.

(C) Impedance of SE-LCO interfaces without coating (0 nm) versus Li<sub>4</sub>Ti<sub>5</sub>O<sub>12</sub>, LiNbO<sub>3</sub>, and LiTaO<sub>3</sub> (dotted, dashed, and solid lines, respectively) coatings with varying thicknesses. Reproduced from Takada et al.<sup>7</sup> with permission. Copyright 2008, Elsevier.

electrolyte LiBs. This interphase layer can be spontaneously formed *in situ* when two materials come into contact or can be artificially coated before contact. To prevent further reactions between the SE and the electrodes, this interphase layer should fully cover the interface and should be electronically insulating, which accounts for the differences in the electron electrochemical potential and Li chemical potential across the SE-electrode interface.<sup>63</sup> Ion conduction through the interphase layer is essential for low interfacial resistance and ionic transport across the interface. Interphase layers that passivate the SE but are also ionically insulating are undesirable. The Li-LiPON and LiPON-LCO interfaces are examples of desirable type 3 interfaces, where the interfaces are both passivating and ion conducting.

This interface classification helps in understanding the interfaces in ASBs that have good cell performance (Figure 11A). As reviewed in Sections 5.1 and 5.2, one notable successful ASB example is the Li-LiPON-LCO thin-film cell,<sup>4</sup> and another is the graphite-Li-P-S SE-LCO bulk-type cell using LPS, Li<sub>9.6</sub>P<sub>3</sub>S<sub>12</sub>, or other sulfide SEs without metal cations (Figure 11A).<sup>1,2</sup> In these ASBs, the thermodynamic intrinsic stabilities of the LiPON and sulfide SEs are significantly narrower than the operating voltages of over 4 V. In the LiPON-based ASBs, both the Li-LiPON and the

LiPON-LCO/LNMO interfaces rely on the *in situ* formation of type 3 passivating interphase layers (Sections 5.1 and 5.2). Similarly, the compatibility between Li-P-S SEs and the graphite anode is also based on the *in situ* formation of the interphase layer (type 3 interface). The formation of interphase layers as in type 3 interfaces in these cells is supported by the observed capacity loss and low Coulombic efficiencies in the first cycle of electrochemical cycling.<sup>1,2,4,141,142</sup> The interface between these sulfide-based SEs and the LCO cathode is an incompatible type 2 interface, and thus an interfacial coating must be applied to convert it to a compatible type 3 interface (Section 5.4).

#### 5.4. Strategies for Enabling Interface Compatibility

On the basis of the understanding of interface types, the selection of SE-electrode pairs and the design of an ASB cell should emphasize the ability to form stable passivating layers rather than only the electrochemical stability of the SEs. While a type 1 interface is ideal, it may be difficult to achieve between most existing SIC SEs and high-energy-density electrodes (e.g., Li metal anode and high-voltage cathodes). Type 3 interfaces, where the interphase formed *in situ* passivates the SE through a mechanism similar to the SEI in commercial LiBs, are desired. This interphase layer formed *in situ* should have decent Li<sup>+</sup> conductivity to maintain low interfacial resistance in addition to electronic insulation and uniform interfacial coverage for good passivation. However, given the limited choice of SEs and electrodes that spontaneously form a type 3 compatible interface, interface engineering such as the application of coating layers is often required to convert an incompatible type 2 interface to a compatible type 3 interface.

For example, the type 2 interfaces of sulfide SE and oxide cathode exhibit poor stability, leading to thick decomposition layers and high interfacial resistance (Section 5.2). Li metal oxide coatings, including Li<sub>2</sub>SiO<sub>3</sub>,<sup>6</sup> LiTaO<sub>3</sub>,<sup>7</sup> Li<sub>3</sub>PO<sub>4</sub>,<sup>143,144</sup> Li<sub>4</sub>Ti<sub>5</sub>O<sub>12</sub>,<sup>145</sup> and LiNbO<sub>3</sub>,<sup>1,2,146</sup> have been demonstrated in numerous experimental studies to reduce interfacial resistance between Li-P-S SEs and oxide cathodes by several orders of magnitude (Figure 11C). Thermodynamic calculations confirm that the sulfide SE-LCO interface with applied oxide coating layers is a compatible type 3 interface (Figure 11A).<sup>63,70,71</sup> Computational studies found the intrinsic electrochemical windows of these coating materials are 2–4 V, so the coatings are stable with the cathode (Figure 11B). In addition, the coating layer generally exhibits chemical and electrochemical compatibility with both sulfide SEs and the LCO cathode.<sup>70,71</sup> These thin layers of Li-containing oxide coating materials significantly lower the Li<sup>+</sup> interfacial resistance compared with the thick decomposition layers, and so reduce the overall interfacial resistance (Figure 11C).<sup>7</sup> The coating layer mitigates the chemical and electrochemical reaction between the SE and cathode, and serves as an artificial SEI, converting the incompatible type 2 interface to a compatible type 3 interface.<sup>63,70</sup> Thus, the role of the coating layer is to limit interfacial decomposition rather than to suppress the formation of space charge layers as previously speculated.<sup>7</sup> Recently, Guo and co-workers demonstrated the LATP SE, which has a suitable electrochemical window (Figure 8A) and high ionic conductivity, as a good cathode coating layer<sup>147</sup>. Using the same materials requirements, thermodynamic calculations were performed to predict new coating layers that enable interfacial compatibility in ASBs.<sup>63,70,71,148,149</sup>

The placement of the coating layers is also important. Composite electrode materials have a complex microstructure comprised of a mixture of the SE, the active electrode material, binder, and electron-conducting additives such as carbon. To protect SEs from electrochemical decomposition and to stabilize the

SE-electrode interface, the coating layer should be applied between the SE and active electrode material and between the SE and carbon.<sup>64,106,148</sup> The coating layer should be electronically insulating to prevent the electrochemical decomposition of the SE, similar to the passivation mechanism in type 3 interfaces and SEI layer (Section 5.3).<sup>63</sup> Although the coating layer is often applied on the cathode active material, it is essential to maintain electronic conduction pathways between the active materials and the current collector. Further studies on the application and engineering of interfacial coating layers in the composite electrodes are still needed.

On the anode side, an incompatible type 2 interface forms between Li metal anode and SEs containing metal cations, due to the formation of MIEC metallic phases (Sections 4 and 5.1). A type 3 interface forms between the Li metal anode and SE materials with no metal cations, such as LiPON, Li<sub>7</sub>P<sub>3</sub>S<sub>11</sub>, or Li<sub>6</sub>PS<sub>5</sub>Cl.<sup>107,108,121</sup> Unfortunately, there is a limited choice of SEs that simultaneously exhibit Li metal compatibility and high Li<sup>+</sup> conductivity. Engineering the interface by applying a coating layer has been demonstrated to improve stability and compatibility with the Li metal anode. Applying coating layers of Li-compatible SEs, such as LiPON and LPS, on Li metal have been demonstrated to form a type 3 compatible interface.<sup>150</sup> In addition to these SEs, other coating materials that do not contain metal cations may also be implemented to avoid the formation of MIEC phases (type 2 interface). For example, an artificial SEI layer of Li<sub>3</sub>PO<sub>4</sub> on the Li metal anode was demonstrated with good performance by Guo and co-workers.<sup>151</sup> Using first-principles computation, Miara et al. discovered Li<sub>9</sub>S<sub>3</sub>N as a protective coating layer for Li metal anodes.<sup>152</sup> Recently, Cui and co-workers demonstrated a nonporous layer of Li<sub>3</sub>N as an artificial SEI layer to protect the Li metal anode.<sup>153</sup>

In a recent first-principles computational study, Mo and co-workers discovered that many Li-containing nitrides that contain metal cations are thermodynamically stable against Li metal (Section 4.3).<sup>101</sup> This discovery significantly broadens the materials choice for Li metal anode protection to include materials with metal cations.<sup>101</sup> Many of these Li metal stable nitride materials can be used as protective coatings on a Li metal anode.<sup>153</sup> In the same study, Mo and co-workers also proposed an interfacial engineering approach of enriching nitrogen content at the SE-Li metal interface to convert type 2 interfaces to type 3 interfaces.<sup>101</sup> Unlike in chalcogenide or halide chemistries, in which the metal cations are reduced to metallic MIEC interphases upon Li metal contact, metal cations in the presence of high nitrogen content form nitride compounds, which are stable against Li metal and serve as a passivating layer. This local enriching of nitrogen content can be achieved through surface nitriding treatments, or by the incorporation of nitrogen-rich materials as electrolyte additives. Recently, experimental work using lithium azide additives was shown to significantly improve the stability of the Li metal anode.<sup>154</sup>

## 6. Concluding Remarks and Perspective

In this review, we present recent advancements in computational techniques with emphases on AIMD simulations and database-enabled thermodynamic calculations, and we highlight their applications in studying SE materials and their interfaces with electrodes in ASBs. Implementation of these new techniques has significantly advanced understanding of fast ion diffusion mechanisms in SIC materials, the electrochemical stability of SE materials, and interfacial compatibility between SEs and electrodes in ASBs. On the basis of this understanding, design principles were

established for the development of new SE materials with fast ionic diffusion and wide electrochemical windows, and for the engineering of SE-electrode interfaces with good compatibility. Following these established design principles, multiple novel SE materials and interface engineering approaches were discovered in computational studies and were confirmed in experiments. These computational studies exemplify the spirit of the MGI in addressing materials problems and in accelerating the design and discovery of new materials for ASBs. Moreover, these computational approaches are also applicable in the study of materials and interfaces in new technologies other than solid-state batteries.

However, major research efforts are still required to achieve a comprehensive set of design principles for fast ion conductors. The design principles for SE materials reviewed in [Section 3.2](#) largely emphasize a low migration energy barrier but do not fully consider the pre-exponential factor of the Arrhenius relation, which is related to several factors, including anion polarizability, lattice softness, mobile carrier concentration, and the ordering of the mobile-ion sublattice.<sup>42,77</sup> Further work is needed to understand these factors and their influence on ionic conduction in materials. Due to the lack of simple, comprehensive design principles, first-principles computation as described in [Section 3.3](#) is still required to identify specific materials compositions and structures as fast ionic conductors. For example, many SE materials require aliovalent doping or substitution to change Li content for achieving optimal ionic conductivity and performance, and so a significant number of dopants and compositions are often explored experimentally to identify the compositions with optimal properties.<sup>78</sup> While this experimental exploration can be accelerated by computational approaches, extensive calculations for a large number of dopants and compositions are still required to identify the optimal SE composition from a given starting structure (e.g., NASICON or garnet). This extensive exploration is computationally expensive when assessing diffusional properties, because AIMD simulations require significant computation costs for each specific composition. Therefore, a predictive model that requires only a small computational cost to predict optimal doped compositions would greatly accelerate the design and optimization of SE materials. This type of model may be based on the descriptors that relate the diffusional properties for a wide range of materials and compositions. However, these descriptors for fast ion conductors are still lacking. Identifying such descriptors may require an understanding of composition-structure-property relationships over a broad materials space, which may be provided by high-throughput computation combined with data-driven approaches.

To be successfully used in ASBs, SEs must simultaneously satisfy multiple requirements in addition to high ionic conductivity and good electrochemical stability. The synthesis, processing, and manufacturing of the SE must be cost effective on a large scale. In particular, air and moisture stabilities of SEs are crucial for the low-cost manufacturing of ASBs, and for enabling solution-based processing to achieve a high loading of active electrode material.<sup>106,155</sup> Air and moisture stability should be emphasized in the future development of SEs, in addition to ionic conductivity and electrochemical stability. In addition, the SE may need particular mechanical properties to retain physical contact with the electrodes after repeated voltage cycling, where both electrodes undergo significant volume changes.<sup>141,156</sup> From the electrode side, the development of a zero-strain cathode may also be a potential alternative. Furthermore, the mechanism of Li dendrite penetration through SEs, which has been widely observed, needs to be understood to enable the Li metal anode in ASBs.

Addressing the challenges at solid-solid interfaces in ASBs should be a research priority. Many studies in this review highlight the importance of interface compatibility of SEs with electrodes. Computational and experimental studies reported the formation of interphase layers between SEs and electrodes, and revealed that these layers define the interface compatibility, disproving earlier myths that SEs are thermodynamically stable against Li metal or high-voltage cathodes. Therefore, as in the case of LiBs with liquid electrolyte, SEI formation should be carefully considered in materials selection, engineering, and processing of ASBs. Given the limited SE and electrode combinations that are compatible, interface engineering is crucial to enable compatible interfaces for high-performance ASBs. For example, an interface engineering approach that leads to spontaneous formation of a stable, ion-conducting, and passivating interphase layer between the SE and electrode is desired.<sup>101</sup> Integrated experimental and computational studies will play a crucial role in the continued development of economical and scalable interfacial engineering approaches for realizing compatible interfaces in ASBs.

Finally, the great need for R&D of new materials and interfaces requires further advancements in computational techniques. While the database-enabled thermodynamic calculations of interface thermodynamics reviewed here provide significant understanding of materials stability and interface compatibility, these approaches still rely on bulk-phase energetics and properties to approximate interfaces. These calculations based on bulk thermodynamics may not fully reflect the actual atomic structure, stoichiometry, chemistry, defects, or microstructures at the interface. While computational studies were performed for the defects in SEs and interfaces,<sup>49–51</sup> the atomistic-scale diffusion mechanisms in amorphous SEs, grain boundaries, and SE-electrode interfaces are still largely unclear. To model the ion diffusion in amorphous materials and at the interfaces, large-scale atomistic modeling at the length scale of 1–100 nm is needed. However, current interatomic potentials may not be adequate, because describing complex atomistic configurations and diverse chemical environments in amorphous materials and interfaces may require the accuracy and versatility of DFT methods. In addition, a major frontier is using computation based on machine learning to guide the synthesis and processing of SEs and ASBs, which still largely depend on trial and error. To achieve enhanced understanding of solid interfaces, it is also important to consider a wide variety of kinetic processes affecting interfacial structures, interfacial Li<sup>+</sup> transport, Li dendrite growth, and mechanical failure. As computational techniques develop further, computational modeling with detailed consideration of kinetics, spanning a range of time and length scales, will further advance understanding and predictive design of materials and interfaces in ASBs.

## ACKNOWLEDGMENTS

The authors acknowledge support from the U.S. Department of Energy, Office of Energy Efficiency and Renewable Energy, under award nos. DE-EE0006860 and DE-EE0007807, and computational resources from the University of Maryland supercomputing facilities and the Maryland Advanced Research Computing Center (MARCC).

## AUTHOR CONTRIBUTIONS

Conceptualization, Y.M.; Visualization, A.M.N., Y.Z., and Y.M.; Writing – Original Draft, Y.M. and A.M.N.; Writing – Review & Editing, A.M.N., Y.M., Y.Z., X.H., and Q.B.; Funding Acquisition, Y.M.; Supervision, Y.M.

## REFERENCES

1. Kamaya, N., Homma, K., Yamakawa, Y., Hirayama, M., Kanno, R., Yonemura, M., Kamiyama, T., Kato, Y., Hama, S., Kawamoto, K., et al. (2011). A lithium superionic conductor. *Nat. Mater.* **10**, 682.
2. Kato, Y., Hori, S., Saito, T., Suzuki, K., Hirayama, M., Mitsui, A., Yonemura, M., Iba, H., and Kanno, R. (2016). High-power all-solid-state batteries using sulfide superionic conductors. *Nat. Energy* **1**, 16030.
3. Han, X., Gong, Y., Fu, K., He, X., Hitz, G.T., Dai, J., Pearse, A., Liu, B., Wang, H., Rubloff, G., et al. (2017). Negating interfacial impedance in garnet-based solid-state Li metal batteries. *Nat. Mater.* **16**, 572–579.
4. Li, J., Ma, C., Chi, M., Liang, C., and Dudney, N.J. (2015). Solid electrolyte: the key for high-voltage lithium batteries. *Adv. Energy Mater.* **5**, 1–6.
5. Hu, Y.-S. (2016). Batteries: getting solid. *Nat. Energy* **1**, 16042.
6. Sakuda, A., Hayashi, A., and Tatsumisago, M. (2010). Interfacial observation between  $\text{LiCoO}_2$  electrode and  $\text{Li}_2\text{S}-\text{P}_2\text{S}_5$  solid electrolytes of all-solid-state lithium secondary batteries using transmission electron microscopy. *Chem. Mater.* **22**, 949–956.
7. Takada, K., Ohta, N., Zhang, L., Fukuda, K., Sakaguchi, I., Ma, R., Osada, M., and Sasaki, T. (2008). Interfacial modification for high-power solid-state lithium batteries. *Solid State Ionics* **179**, 1333–1337.
8. Wadia, C. (2011). Materials Genome Initiative for Global Competitiveness (National Science and Technology Council), pp. 1–18.
9. Yang, K., Setyawan, W., Wang, S., Buongiorno Nardelli, M., and Curtarolo, S. (2012). A search model for topological insulators with high-throughput robustness descriptors. *Nat. Mater.* **11**, 614–619.
10. Wang, S., Wang, Z., Setyawan, W., Mingo, N., and Curtarolo, S. (2011). Assessing the thermoelectric properties of sintered compounds via high-throughput Ab-initio calculations. *Phys. Rev. X* **1**, 021012.
11. Curtarolo, S., Hart, G.L.W., Nardelli, M.B., Mingo, N., Sanvito, S., and Levy, O. (2013). The high-throughput highway to computational materials design. *Nat. Mater.* **12**, 191–201.
12. Yu, L., and Zunger, A. (2012). Identification of potential photovoltaic absorbers based on first-principles spectroscopic screening of materials. *Phys. Rev. Lett.* **108**, 068701.
13. Greeley, J., Jaramillo, T.F., Bonde, J., Chorkendorff, I., and Nørskov, J.K. (2006). Computational high-throughput screening of electrocatalytic materials for hydrogen evolution. *Nat. Mater.* **5**, 909–913.
14. Nørskov, J.K., Bligaard, T., Rossmeisl, J., and Christensen, C.H. (2009). Towards the computational design of solid catalysts. *Nat. Chem.* **1**, 37–46.
15. Jain, A., Shin, Y., and Persson, K.A. (2016). Computational predictions of energy materials using density functional theory. *Nat. Rev. Mater.* **1**, 1–13.
16. Urban, A., Seo, D.H., and Ceder, G. (2016). Computational understanding of Li-ion batteries. *npj Comput. Mater.* **2**, 16002.
17. Deng, Z., Mo, Y., and Ong, S.P. (2016). Computational studies of solid-state alkali conduction in rechargeable alkali-ion batteries. *NPG Asia Mater.* **8**, e254.
18. Islam, M.S., and Fisher, C.A.J. (2014). Lithium and sodium battery cathode materials: computational insights into voltage, diffusion and nanostructural properties. *Chem. Soc. Rev.* **43**, 185–204.
19. Shi, S., Gao, J., Liu, Y., Zhao, Y., Wu, Q., Ju, W., Ouyang, C., and Xiao, R. (2016). Multi-scale computation methods: their applications in lithium-ion battery research and development. *Chin. Phys. B* **25**, 18212.
20. Bai, Q., Chen, H., Yang, L., and Mo, Y. (2018). Computational studies of electrode materials in sodium-ion batteries. *Adv. Energy Mater.* **8**, 1702998.
21. Jain, A., Ong, S.P., Hautier, G., Chen, W., Richards, W.D., Dacek, S., Cholia, S., Gunter, D., Skinner, D., Ceder, G., et al. (2013). Commentary: the materials project: a materials genome approach to accelerating materials innovation. *APL Mater.* **1**, 011002.
22. Henkelman, G., Uberuaga, B.P., and Jónsson, H. (2000). Climbing image nudged elastic band method for finding saddle points and minimum energy paths. *J. Chem. Phys.* **113**, 9901–9904.
23. Wang, Y., Richards, W.D., Ong, S.P., Miara, L.J., Kim, J.C., Mo, Y., and Ceder, G. (2015). Design principles for solid-state lithium superionic conductors. *Nat. Mater.* **14**, 1026–1031.
24. Michel, K.J., and Wolverton, C. (2014). Symmetry building Monte Carlo-based crystal structure prediction. *Comput. Phys. Commun.* **185**, 1389–1393.
25. Michel, K.J., and Ozoliņš, V. (2011). Native defect concentrations in  $\text{NaAlH}_4$  and  $\text{Na}_3\text{AlH}_6$ . *J. Phys. Chem. C* **115**, 21443–21453.
26. Michel, K.J., and Ozoliņš, V. (2011). Site substitution of Ti in  $\text{NaAlH}_4$  and  $\text{Na}_3\text{AlH}_6$ . *J. Phys. Chem. C* **115**, 21454–21464.
27. Holzwarth, N.A.W., Lepley, N.D., and Du, Y.A. (2011). Computer modeling of lithium phosphate and thiophosphate electrolyte materials. *J. Power Sources* **196**, 6870–6876.
28. Holzwarth, N.A.W. (2014). First principles modeling of electrolyte materials in all-solid-state batteries. *Phys. Procedia* **57**, 29–37.
29. Xiao, P., and Henkelman, G. (2018). Kinetic Monte Carlo study of Li intercalation in  $\text{LiFePO}_4$ . *ACS Nano* **12**, 844–851.
30. Henkelman, G., and Jónsson, H. (2001). Long time scale kinetic Monte Carlo simulations without lattice approximation and predefined event table. *J. Chem. Phys.* **115**, 9657–9666.
31. Yao, Z., Kim, S., Michel, K., Zhang, Y., Aykol, M., and Wolverton, C. (2018). Stability and conductivity of cation- and anion-substituted  $\text{LiBH}_4$ -based solid-state electrolytes. *Phys. Rev. Mater.* **2**, 65402.
32. Michel, K.J., and Ozoliņš, V. (2011). Vacancy diffusion in  $\text{NaAlH}_4$  and  $\text{Na}_3\text{AlH}_6$ . *J. Phys. Chem. C* **115**, 21465–21472.
33. He, X., and Mo, Y. (2015). Accelerated materials design of  $\text{Na}_{0.5}\text{Bi}_{0.5}\text{TiO}_3$  oxygen ionic conductors based on first principles calculations. *Phys. Chem. Chem. Phys.* **17**, 18035–18044.
34. He, X., Zhu, Y., and Mo, Y. (2017). Origin of fast ion diffusion in super-ionic conductors. *Nat. Commun.* **8**, 1–7.
35. Bai, Q., He, X., Zhu, Y., and Mo, Y. (2018). First-principles study of oxyhydride  $\text{H}^+$  ion conductors: toward facile anion conduction in oxide-based materials. *ACS Appl. Energy Mater.* **1**, 1626–1634.
36. Richards, W.D., Wang, Y., Miara, L.J., Kim, J.C., and Ceder, G. (2016). Design of  $\text{Li}_{1+2x}\text{Zn}_{1-x}\text{PS}_4$ , a new lithium ion conductor. *Energy Environ. Sci.* **9**, 3272–3278.
37. Jalem, R., Yamamoto, Y., Shiiiba, H., Nakayama, M., Munakata, H., Kasuga, T., and Kanamura, K. (2013). Concerted migration mechanism in the Li ion dynamics of garnet-type  $\text{Li}_7\text{La}_3\text{Zr}_2\text{O}_{12}$ . *Chem. Mater.* **25**, 425–430.
38. Mo, Y., Ong, S.P., and Ceder, G. (2012). First principles study of the  $\text{Li}_{10}\text{GeP}_2\text{S}_12$  lithium super ionic conductor material. *Chem. Mater.* **24**, 15–17.
39. He, X., Zhu, Y., Epstein, A., and Mo, Y. (2018). Statistical variances of diffusional properties from ab initio molecular dynamics simulations. *npj Comput. Mater.* **4**, 18.
40. de Klerk, N.J.J., van der Maas, E., and Wagemaker, M. (2018). Analysis of diffusion in solid-state electrolytes through MD simulations, improvement of the Li-ion conductivity in  $\beta\text{-Li}_3\text{PS}_4$  as an example. *ACS Appl. Energy Mater.* **1**, 3230–3242.
41. Deng, Z., Zhu, Z., Chu, I.-H., and Ong, S.P. (2017). Data-driven first-principles methods for the study and design of alkali superionic conductors. *Chem. Mater.* **29**, 281–288.
42. Kraft, M.A., Culver, S.P., Calderon, M., Böcher, F., Krauskopf, T., Senyshyn, A., Dietrich, C., Zevalkink, A., Janek, J., and Zeier, W.G. (2017). Influence of lattice polarizability on the ionic conductivity in the lithium superionic argyrodites  $\text{Li}_x\text{PS}_5\text{X}$  ( $\text{X} = \text{Cl}, \text{Br}, \text{I}$ ). *J. Am. Chem. Soc.* **139**, 10909–10918.
43. Culver, S.P., Koerver, R., Krauskopf, T., and Zeier, W.G. (2018). Designing ionic conductors: the interplay between structural phenomena and interfaces in thiophosphate-based solid-state batteries. *Chem. Mater.* **30**, 4179–4192.
44. Krauskopf, T., Pompe, C., Kraft, M.A., and Zeier, W.G. (2017). Influence of lattice dynamics on  $\text{Na}^+$  transport in the solid electrolyte  $\text{Na}_3\text{PS}_{4-x}\text{Se}_x$ . *Chem. Mater.* **29**, 8859–8869.

45. Muy, S., Bachman, J.C., Giordano, L., Chang, H.H., Abernathy, D.L., Bansal, D., Delaire, O., Hori, S., Kanno, R., Maglia, F., et al. (2018). Tuning mobility and stability of lithium ion conductors based on lattice dynamics. *Energy Environ. Sci.* 11, 850–859.
46. Thangadurai, V., Pinzarlu, D., Narayanan, S., and Baral, A.K. (2015). Fast solid-state Li ion conducting garnet-type structure metal oxides for energy storage. *J. Phys. Chem. Lett.* 6, 292–299.
47. Bernstein, N., Johannes, M.D., and Hoang, K. (2012). Origin of the structural phase transition in  $\text{Li}_7\text{La}_3\text{Zr}_2\text{O}_{12}$ . *Phys. Rev. Lett.* 109, 205702.
48. Chen, Y., Rangasamy, E., Liang, C., and An, K. (2015). Origin of high  $\text{Li}^+$  conduction in doped  $\text{Li}_7\text{La}_3\text{Zr}_2\text{O}_{12}$  garnets. *Chem. Mater.* 27, 5491–5494.
49. KC, S., Longo, R.C., Xiong, K., and Cho, K. (2014). Electrode-electrolyte interface for solid state Li-ion batteries: point defects and mechanical strain. *J. Electrochem. Soc.* 161, F3104–F3110.
50. Santosh, K.C., Longo, R.C., Xiong, K., and Cho, K. (2014). Point defects in garnet-type solid electrolyte ( $\text{c-Li}_7\text{La}_3\text{Zr}_2\text{O}_{12}$ ) for Li-ion batteries. *Solid State Ionics* 261, 100–105.
51. Stegmaier, S., Voss, J., Reuter, K., and Luntz, A.C. (2017).  $\text{Li}^+$  defects in a solid-state Li ion battery: theoretical insights with a  $\text{Li}_3\text{OCl}$  electrolyte. *Chem. Mater.* 29, 4330–4340.
52. Al-Qawasmeh, A., and Holzwarth, N.A.W. (2017).  $\text{Li}_{14}\text{P}_2\text{O}_3\text{N}_6$  and  $\text{Li}_7\text{PN}_4$ : computational study of two nitrogen rich crystalline LiPON electrolyte materials. *J. Power Sources* 364, 410–419.
53. Rush, L.E., and Holzwarth, N.A.W. (2016). First principles investigation of the structural and electrochemical properties of  $\text{Na}_4\text{P}_2\text{S}_6$  and  $\text{Li}_4\text{P}_2\text{S}_6$ . *Solid State Ionics* 286, 45–50.
54. Curtarolo, S., Setyawan, W., Hart, G.L.W., Jahnatek, M., Chepulskii, R.V., Taylor, R.H., Wang, S., Xue, J., Yang, K., Levy, O., et al. (2012). AFLOW: an automatic framework for high-throughput materials discovery. *Comput. Mater. Sci.* 58, 218–226.
55. Kirklin, S., Saal, J.E., Meredig, B., Thompson, A., Doak, J.W., Aykol, M., Rühl, S., and Wolverton, C. (2015). The open quantum materials database (OQMD): assessing the accuracy of DFT formation energies. *npj Comput. Mater.* 1, 15010.
56. Ong, S.P., Wang, L., Kang, B., and Ceder, G. (2008). Li–Fe–P–O<sub>2</sub> phase diagram from first principles calculations. *Chem. Mater.* 20, 1798–1807.
57. Sun, W., Dacek, S.T., Ong, S.P., Hautier, G., Jain, A., Richards, W.D., Gamst, A.C., Persson, K.A., and Ceder, G. (2016). The thermodynamic scale of inorganic crystalline metastability. *Sci. Adv.* 2, e1600225.
58. Miara, L.J., Ong, S.P., Mo, Y., Richards, W.D., Park, Y., Lee, J.M., Lee, H.S., and Ceder, G. (2013). Effect of Rb and Ta doping on the ionic conductivity and stability of the garnet  $\text{Li}_{7+2x-y}(\text{La}_{3-x}\text{Rb}_x)(\text{Zr}_{2-y}\text{Ta}_y)\text{O}_{12}$  ( $0 \leq x \leq 0.375$ ,  $0 \leq y \leq 1$ ) superionic conductor: a first principles investigation. *Chem. Mater.* 25, 3048–3055.
59. Wang, Y., Richards, W.D., Bo, S.H., Miara, L.J., and Ceder, G. (2017). Computational prediction and evaluation of solid-state sodium superionic conductors  $\text{Na}_7\text{P}_3\text{X}_{12}$  ( $\text{X} = \text{O}, \text{S}, \text{Se}$ ). *Chem. Mater.* 29, 7475–7482.
60. Kang, S., Mo, Y., Ong, S.P., and Ceder, G. (2014). Nanoscale stabilization of sodium oxides: implications for  $\text{Na}-\text{O}_2$  batteries. *Nano Lett.* 14, 1016–1020.
61. Hautier, G., Ong, S.P., Jain, A., Moore, C.J., and Ceder, G. (2012). Accuracy of density functional theory in predicting formation energies of ternary oxides from binary oxides and its implication on phase stability. *Phys. Rev. B* 85, 155208.
62. Ong, S.P., Mo, Y., Richards, W.D., Miara, L., Lee, H.S., and Ceder, G. (2013). Phase stability, electrochemical stability and ionic conductivity of the  $\text{Li}_{10+\delta}\text{MP}_2\text{X}_{12}$  ( $\text{M} = \text{Ge}, \text{Si}, \text{Sn}, \text{Al}$  or  $\text{P}$ , and  $\text{X} = \text{O}, \text{S}$  or  $\text{Se}$ ) family of superionic conductors. *Energy Environ. Sci.* 6, 148–156.
63. Zhu, Y., He, X., and Mo, Y. (2015). Origin of outstanding stability in the lithium solid electrolyte materials: insights from thermodynamic analyses based on first-principles calculations. *ACS Appl. Mater. Interfaces* 7, 23685–23693.
64. Han, F., Zhu, Y., He, X., Mo, Y., and Wang, C. (2016). Electrochemical stability of  $\text{Li}_{10}\text{GeP}_2\text{S}_{12}$  and  $\text{Li}_7\text{La}_3\text{Zr}_2\text{O}_{12}$  solid electrolytes. *Adv. Energy Mater.* 6, 1–9.
65. Peljo, P., and Girault, H. (2018). Electrochemical potential window of battery electrolytes: the HOMO-LUMO misconception. *Energy Environ. Sci.* <https://doi.org/10.1039/C8EE01286E>.
66. Ong, S.P., Andreussi, O., Wu, Y., Marzari, N., and Ceder, G. (2011). Electrochemical windows of room-temperature ionic liquids from molecular dynamics and density functional theory calculations. *Chem. Mater.* 23, 2979–2986.
67. Han, Y.-K., Yoo, J., and Yim, T. (2017). Computational screening of phosphite derivatives as high-performance additives in high-voltage Li-ion batteries. *RSC Adv.* 7, 20049–20056.
68. Jain, A., Hautier, G., Ong, S.P., Dacek, S., and Ceder, G. (2015). Relating voltage and thermal safety in Li-ion battery cathodes: a high-throughput computational study. *Phys. Chem. Chem. Phys.* 17, 5942–5953.
69. Miara, L.J., Richards, W.D., Wang, Y.E., and Ceder, G. (2015). First-principles studies on cation dopants and electrolyte|cathode interphases for lithium garnets. *Chem. Mater.* 27, 4040–4047.
70. Zhu, Y., He, X., and Mo, Y. (2016). First principles study on electrochemical and chemical stability of solid electrolyte–electrode interfaces in all-solid-state Li-ion batteries. *J. Mater. Chem. A* 4, 3253–3266.
71. Richards, W.D., Miara, L.J., Wang, Y., Kim, J.C., and Ceder, G. (2016). Interface stability in solid-state batteries. *Chem. Mater.* 28, 266–273.
72. Weber, D.A., Senyshyn, A., Weldert, K.S., Wenzel, S., Zhang, W., Kaiser, R., Berends, S., Janek, J., and Zeier, W.G. (2016). Structural insights and 3D diffusion pathways within the lithium superionic conductor  $\text{Li}_{10}\text{GeP}_2\text{S}_{12}$ . *Chem. Mater.* 28, 5905–5915.
73. Adams, S., and Prasada Rao, R. (2012). Structural requirements for fast lithium ion migration in  $\text{Li}_{10}\text{GeP}_2\text{S}_{12}$ . *J. Mater. Chem.* 22, 7687.
74. Kwon, O., Hirayama, M., Suzuki, K., Kato, Y., Saito, T., Yonemura, M., Kamiyama, T., and Kanno, R. (2015). Synthesis, structure, and conduction mechanism of the lithium superionic conductor  $\text{Li}_{10+\delta}\text{Ge}_{1+\delta}\text{P}_{2-\delta}\text{S}_{12}$ . *J. Mater. Chem. A* 3, 438–446.
75. Xu, M., Ding, J., and Ma, E. (2012). One-dimensional stringlike cooperative migration of lithium ions in an ultrafast ionic conductor. *Appl. Phys. Lett.* 101, 031901.
76. Richards, W.D., Tsujimura, T., Miara, L.J., Wang, Y., Kim, J.C., Ong, S.P., Uechi, I., Suzuki, N., and Ceder, G. (2016). Design and synthesis of the superionic conductor  $\text{Na}_{10}\text{SnP}_2\text{S}_{12}$ . *Nat. Commun.* 7, 11009.
77. Hull, S. (2004). Superionics: crystal structures and conduction processes. *Rep. Prog. Phys.* 67, 1233–1314.
78. Bachman, J.C., Muy, S., Grimaud, A., Chang, H.H., Pour, N., Lux, S.F., Paschos, O., Maglia, F., Lupart, S., Lamp, P., et al. (2016). Inorganic solid-state electrolytes for lithium batteries: mechanisms and properties governing ion conduction. *Chem. Rev.* 116, 140–162.
79. Kaup, K., Lalere, F., Huq, A., Shyamsunder, A., Adermann, T., Hartmann, P., and Nazar, L.F. (2018). Correlation of structure and fast ion conductivity in the solid solution series  $\text{Li}_{1+2x}\text{Zn}_{1-x}\text{PS}_4$ . *Chem. Mater.* 30, 592–596.
80. Suzuki, N., Richards, W.D., Wang, Y., Miara, L.J., Kim, J.C., Jung, I.-S., Tsujimura, T., and Ceder, G. (2018). Synthesis and electrochemical properties of  $\text{I}4$ -type  $\text{Li}_{1+2x}\text{Zn}_{1-x}\text{PS}_4$  solid electrolyte. *Chem. Mater.* 30, 2236–2244.
81. Hori, S., Suzuki, K., Hirayama, M., Kato, Y., Saito, T., Yonemura, M., and Kanno, R. (2014). Synthesis, structure, and ionic conductivity of solid solution,  $\text{Li}_{10+\delta}\text{M}_{1+\delta}\text{P}_{2-\delta}\text{S}_{12}$  ( $\text{M} = \text{Si}, \text{Sn}$ ). *Faraday Discuss.* 176, 83–94.
82. Bron, P., Johansson, S., Zick, K., Der Günne, J.S.A., Dehnen, S., and Roling, B. (2013).  $\text{Li}_{10}\text{SnP}_2\text{S}_{12}$ : an affordable lithium superionic conductor. *J. Am. Chem. Soc.* 135, 15694–15697.
83. Kuhn, A., Gerbig, O., Zhu, C., Falkenberg, F., Maier, J., and Lotsch, B.V. (2014). A new ultrafast superionic Li-conductor: ion dynamics in  $\text{Li}_{11}\text{Si}_2\text{PS}_12$  and comparison with other tetragonal LGPS-type electrolytes. *Phys. Chem. Chem. Phys.* 16, 14669–14674.
84. Whiteley, J.M., Woo, J.H., Hu, E., Nam, K.-W., and Lee, S.-H. (2014). Empowering the lithium metal battery through a silicon-based superionic conductor. *J. Electrochem. Soc.* 161, A1812–A1817.
85. Kato, Y., Saito, R., Sakano, M., Mitsui, A., Hirayama, M., and Kanno, R. (2014). Synthesis, structure and lithium ionic conductivity of

- solid solutions of  $\text{Li}_{10}(\text{Ge}_{1-x}\text{M}_x)\text{P}_2\text{S}_{12}$  ( $\text{M} = \text{Si}, \text{Sn}$ ). *J. Power Sources* 271, 60–64.
86. Krauskopf, T., Culver, S.P., and Zeier, W.G. (2018). Bottleneck of diffusion and inductive effects in  $\text{Li}_{10}\text{Ge}_{1-x}\text{Sn}_x\text{P}_2\text{S}_{12}$ . *Chem. Mater.* 30, 1791–1798.
87. Bai, Q., Zhu, Y., He, X., Wachsmann, E., and Mo, Y. (2018). First principles hybrid functional study of small polarons in doped  $\text{SrCeO}_3$  perovskite: towards computation design of materials with tailored polaron. *Ionics*, 24, 1139–1151.
88. Canepa, P., Bo, S.H., Sai Gautam, G., Key, B., Richards, W.D., Shi, T., Tian, Y., Wang, Y., Li, J., and Ceder, G. (2017). High magnesium mobility in ternary spinel chalcogenides. *Nat. Commun.* 8, 1759.
89. Zhang, L., Yang, K., Mi, J., Lu, L., Zhao, L., Wang, L., Li, Y., and Zeng, H. (2015).  $\text{Na}_3\text{PS}_4$ : a novel chalcogenide solid electrolyte with high ionic conductivity. *Adv. Energy Mater.* 5, 2–6.
90. Chu, I.H., Kompella, C.S., Nguyen, H., Zhu, Z., Hy, S., Deng, Z., Meng, Y.S., and Ong, S.P. (2016). Room-temperature all-solid-state rechargeable sodium-ion batteries with a Cl-doped  $\text{Na}_3\text{PS}_4$  superionic conductor. *Sci. Rep.* 6, 1–10.
91. Avdeev, M., Sale, M., Adams, S., and Rao, R.P. (2012). Screening of the alkali-metal ion containing materials from the inorganic crystal structure database (ICSD) for high ionic conductivity pathways using the bond valence method. *Solid State Ionics* 225, 43–46.
92. Xiao, R., Li, H., and Chen, L. (2015). High-throughput design and optimization of fast lithium ion conductors by the combination of bond-valence method and density functional theory. *Sci. Rep.* 5, 14227.
93. Sendek, A.D., Yang, Q., Cubuk, E.D., Duerloo, K.-A.N., Cui, Y., and Reed, E.J. (2017). Holistic computational structure screening of more than 12 000 candidates for solid lithium-ion conductor materials. *Energy Environ. Sci.* 10, 306–320.
94. Wang, X., Xiao, R., Li, H., and Chen, L. (2017). Oxysulfide LiAlSO: a lithium superionic conductor from first principles. *Phys. Rev. Lett.* 118, 195901.
95. Hautier, G., Fischer, C., Ehrlacher, V., Jain, A., and Ceder, G. (2011). Data mined ionic substitutions for the discovery of new compounds. *Inorg. Chem.* 50, 656–663.
96. Zhu, Z., Chu, I.H., and Ong, S.P. (2017).  $\text{Li}_2\text{Y}(\text{PS}_4)_2$  and  $\text{Li}_5\text{PS}_4\text{Cl}_2$ : new lithium superionic conductors predicted from silver thiophosphates using efficiently tiered Ab initio molecular dynamics simulations. *Chem. Mater.* 29, 2474–2484.
97. Ohta, S., Kobayashi, T., and Asaoka, T. (2011). High lithium ionic conductivity in the garnet-type oxide  $\text{Li}_{7-x}\text{La}_3(\text{Zr}_{2-x}\text{Nb}_x)\text{O}_{12}$  ( $x = 0\text{--}2$ ). *J. Power Sources* 196, 3342–3345.
98. Han, F., Gao, T., Zhu, Y., Gaskell, K.J., and Wang, C. (2015). A battery made from a single material. *Adv. Mater.* 27, 3473–3483.
99. Manthiram, A., Fu, Y., Chung, S.-H., Zu, C., and Su, Y.-S. (2014). Rechargeable lithium-sulfur batteries. *Chem. Rev.* 114, 11751–11787.
100. Wenzel, S., Randau, S., Leichtweiss, T., Weber, D.A., Sann, J., Zeier, W.G., and Janek, J. (2016). Direct observation of the interfacial instability of the fast ionic conductor  $\text{Li}_{10}\text{GeP}_2\text{S}_{12}$  at the lithium metal anode. *Chem. Mater.* 28, 2400–2407.
101. Zhu, Y., He, X., and Mo, Y. (2017). Strategies based on nitride materials chemistry to stabilize Li metal anode. *Adv. Sci.* 4, 1–11.
102. Bron, P., Roling, B., and Dehnen, S. (2017). Impedance characterization reveals mixed conducting interphases between sulfidic superionic conductors and lithium metal electrodes. *J. Power Sources* 352, 127–134.
103. Goodenough, J.B., and Kim, Y. (2010). Challenges for rechargeable Li batteries. *Chem. Mater.* 22, 587–603.
104. Zhang, W., Leichtweiss, T., Culver, S.P., Koerver, R., Das, D., Weber, D.A., Zeier, W.G., and Janek, J. (2017). The detrimental effects of carbon additives in  $\text{Li}_{10}\text{GeP}_2\text{S}_{12}$ -based solid-state batteries. *ACS Appl. Mater. Interfaces* 9, 35888–35896.
105. Kato, Y., Shiotani, S., Morita, K., Suzuki, K., Hirayama, M., and Kanno, R. (2018). All-solid-state batteries with thick electrode configurations. *J. Phys. Chem. Lett.* 9, 607–613.
106. Park, K.H., Bai, Q., Kim, D.H., Oh, D.Y., Zhu, Y., and Mo, Y. (2018). Design strategies, practical considerations, and new solution processes of sulfide solid electrolytes for all-solid-state batteries. *Adv. Energy Mater.* 8, 1800035.
107. Wenzel, S., Sedlmaier, S.J., Dietrich, C., Zeier, W.G., and Janek, J. (2018). Interfacial reactivity and interphase growth of argyrodite solid electrolytes at lithium metal electrodes. *Solid State Ionics* 318, 102–112.
108. Wenzel, S., Weber, D.A., Leichtweiss, T., Busche, M.R., Sann, J., and Janek, J. (2016). Interphase formation and degradation of charge transfer kinetics between a lithium metal anode and highly crystalline  $\text{Li}_7\text{P}_3\text{S}_{11}$  solid electrolyte. *Solid State Ionics* 286, 24–33.
109. Hakari, T., Deguchi, M., Mitsuhashi, K., Ohta, T., Saito, K., Orikasa, Y., Uchimoto, Y., Kowada, Y., Hayashi, A., and Tatsumisago, M. (2017). Structural and electronic-state changes of a sulfide solid electrolyte during the Li deinsertion-insertion processes. *Chem. Mater.* 29, 4768–4774.
110. Koerver, R., Walther, F., Aygün, I., Sann, J., Dietrich, C., Zeier, W.G., and Janek, J. (2017). Redox-active cathode interphases in solid-state batteries. *J. Mater. Chem. A* 5, 22750–22760.
111. Auvergnot, J., Cassel, A., Ledreuil, J.B., Viallet, V., Seznec, V., and Dedryvère, R. (2017). Interface stability of argyrodite  $\text{Li}_6\text{PS}_5\text{Cl}$  toward  $\text{LiCoO}_2$ ,  $\text{LiNi}_{1/3}\text{Co}_{1/3}\text{Mn}_{1/3}\text{O}_2$ , and  $\text{LiMn}_2\text{O}_4$  in bulk all-solid-state batteries. *Chem. Mater.* 29, 3883–3890.
112. Sathiya, M., Rousse, G., Ramesha, K., Laisa, C.P., Vezin, H., Sougrati, M.T., Doublet, M.L., Foix, D., Gonbeau, D., Walker, W., et al. (2013). Reversible anionic redox chemistry in high-capacity layered-oxide electrodes. *Nat. Mater.* 12, 827–835.
113. Grimaud, A., Hong, W.T., Shao-Horn, Y., and Tarascon, J.-M. (2016). Anionic redox processes for electrochemical devices. *Nat. Mater.* 15, 121.
114. Girishkumar, G., McCloskey, B., Luntz, A.C., Swanson, S., and Wilcke, W. (2010). Lithium-air battery: promise and challenges. *J. Phys. Chem. Lett.* 1, 2193–2203.
115. Mo, Y., Ong, S.P., and Ceder, G. (2011). First-principles study of the oxygen evolution reaction of lithium peroxide in the lithium-air battery. *Phys. Rev. B* 84, 205446.
116. Thompson, T., Yu, S., Williams, L., Schmidt, R.D., Garcia-Mendez, R., Wolfenstein, J., Allen, J.L., Kioupakis, E., Siegel, D.J., and Sakamoto, J. (2017). Electrochemical window of the Li-ion solid electrolyte  $\text{Li}_7\text{La}_3\text{Zr}_2\text{O}_{12}$ . *ACS Energy Lett.* 2, 462–468.
117. Hartmann, P., Leichtweiss, T., Busche, M.R., Schneider, M., Reich, M., Sann, J., Adelhelm, P., and Janek, J. (2013). Degradation of NASICON-type materials in contact with lithium metal: formation of mixed conducting interphases (MCI) on solid electrolytes. *J. Phys. Chem. C* 117, 21064–21074.
118. Nakayama, M., Usui, T., Uchimoto, Y., Wakihara, M., and Yamamoto, M. (2005). Changes in electronic structure upon lithium insertion into the A-site deficient perovskite type oxides  $(\text{Li},\text{La})\text{TiO}_3$ . *J. Phys. Chem. B* 109, 4135–4143.
119. Hua, C., Fang, X., Wang, Z., and Chen, L. (2013). Lithium storage in perovskite lithium lanthanum titanate. *Electrochem. Commun.* 32, 5–8.
120. Wenzel, S., Leichtweiss, T., Krüger, D., Sann, J., and Janek, J. (2015). Interphase formation on lithium solid electrolytes—an *in situ* approach to study interfacial reactions by photoelectron spectroscopy. *Solid State Ionics* 278, 98–105.
121. Schwöbel, A., Hausbrand, R., and Jaegermann, W. (2015). Interface reactions between LiPON and lithium studied by *in-situ* X-ray photoemission. *Solid State Ionics* 273, 51–54.
122. Yu, X., Bates, J.B., Jellison, G.E., and Hart, F.X. (1997). A stable thin-film lithium electrolyte: lithium phosphorus oxynitride. *J. Electrochem. Soc.* 144, 524–532.
123. Bates, J.B., Gruzalski, G.R., Dudney, N.J., Luck, C.F., and Yu, X. (1994). Rechargeable thin-film lithium batteries. *Solid State Ionics* 70–71, 619–628.
124. Wang, B. (1996). Characterization of thin-film rechargeable lithium batteries with lithium cobalt oxide cathodes. *J. Electrochem. Soc.* 143, 3203.
125. Luo, W., Gong, Y., Zhu, Y., Fu, K.K., Dai, J., Lacey, S.D., Wang, C., Liu, B., Han, X., Mo, Y., et al. (2016). Transition from superlithiophobicity to superlithiophilicity of garnet solid-state electrolyte. *J. Am. Chem. Soc.* 138, 12258–12262.

126. Zhao, Y., and Daemen, L.L. (2012). Superionic conductivity in lithium-rich anti-perovskites. *J. Am. Chem. Soc.* 134, 15042–15047.
127. Wood, K.N., Steirer, K.X., Hafner, S.E., Ban, C., Santhanagopalan, S., Lee, S.-H., and Teeter, G. (2018). Operando X-ray photoelectron spectroscopy of solid electrolyte interphase formation and evolution in  $\text{Li}_2\text{S}-\text{P}_2\text{S}_5$  solid-state electrolytes. *Nat. Commun.* 9, 2490.
128. Sakuda, A., Hayashi, A., and Tatsumisago, M. (2013). Sulfide solid electrolyte with favorable mechanical property for all-solid-state lithium battery. *Sci. Rep.* 3, 2–6.
129. Miara, L., Windmüller, A., Tsai, C.L., Richards, W.D., Ma, Q., Uhlenbruck, S., Guillon, O., and Ceder, G. (2016). About the compatibility between high voltage spinel cathode materials and solid oxide electrolytes as a function of temperature. *ACS Appl. Mater. Interfaces* 8, 26842–26850.
130. Park, K., Yu, B.C., Jung, J.W., Li, Y., Zhou, W., Gao, H., Son, S., and Goodenough, J.B. (2016). Electrochemical nature of the cathode interface for a solid-state lithium-ion battery: interface between  $\text{LiCoO}_2$  and garnet- $\text{Li}_2\text{Zr}_2\text{O}_{12}$ . *Chem. Mater.* 28, 8051–8059.
131. Han, F., Yue, J., Chen, C., Zhao, N., Fan, X., Ma, Z., Gao, T., Wang, F., Guo, X., and Wang, C. (2018). Interphase engineering enabled all-ceramic lithium battery. *Joule* 2, 497–508.
132. Visbal, H., Aihara, Y., Ito, S., Watanabe, T., Park, Y., and Doo, S. (2016). The effect of diamond-like carbon coating on  $\text{LiNi}_{0.8}\text{Co}_{0.15}\text{Al}_{0.05}\text{O}_2$  particles for all solid-state lithium-ion batteries based on  $\text{Li}_2\text{S}-\text{P}_2\text{S}_5$  glass-ceramics. *J. Power Sources* 314, 85–92.
133. Kumar, N., Raman, N., and Sundaresan, A. (2014). Synthesis and properties of cobalt sulfide phases:  $\text{Co}_2\text{S}_3$  and  $\text{Co}_9\text{S}_8$ . *Z. Anorg. Allg. Chem.* 640, 1069–1074.
134. Trevey, J.E., Stoldt, C.R., and Lee, S.-H. (2011). High power nanocomposite  $\text{TiS}_2$  cathodes for all-solid-state lithium batteries. *J. Electrochem. Soc.* 158, A1282.
135. Han, F., Yue, J., Fan, X., Gao, T., Luo, C., Ma, Z., Suo, L., and Wang, C. (2016). High-performance all-solid-state lithium-sulfur battery enabled by a mixed-conductive  $\text{Li}_2\text{S}$  nanocomposite. *Nano Lett.* 16, 4521–4527.
136. Yao, X., Huang, N., Han, F., Zhang, Q., Wan, H., Mwizerwa, J.P., Wang, C., and Xu, X. (2017). High-performance all-solid-state lithium-sulfur batteries enabled by amorphous sulfur-coated reduced graphene oxide cathodes. *Adv. Energy Mater.* 7, 1–9.
137. Wang, Z., Santhanagopalan, D., Zhang, W., Wang, F., Xin, H.L., He, K., Li, J., Dudney, N., and Meng, Y.S. (2016). In Situ STEM-EELS observation of nanoscale interfacial phenomena in all-solid-state batteries. *Nano Lett.* 16, 3760–3767.
138. Fingerle, M., Buchheit, R., Sicolo, S., Albe, K., and Hausbrand, R. (2017). Reaction and space charge layer formation at the  $\text{LiCoO}_2$ -LiPON interface: insights on defect formation and ion energy level alignment by a combined surface science-simulation approach. *Chem. Mater.* 29, 7675–7685.
139. Leung, K., Pearse, A.J., Talin, A.A., Fuller, E.J., Rubloff, G.W., and Modine, N.A. (2018). Kinetics-controlled degradation reactions at crystalline LiPON/Li<sub>x</sub>CoO<sub>2</sub> and crystalline LiPON/Li-metal interfaces. *ChemSusChem* 11, 1956–1969.
140. Wenzel, S., Leichtweiss, T., Weber, D.A., Sann, J., Zeier, W.G., and Janek, J. (2016). Interfacial reactivity benchmarking of the sodium ion conductors  $\text{Na}_3\text{PS}_4$  and sodium  $\beta$ -alumina for protected sodium metal anodes and sodium all-solid-state batteries. *ACS Appl. Mater. Interfaces* 8, 28216–28224.
141. Koerver, R., Aygün, I., Leichtweiß, T., Dietrich, C., Zhang, W., Binder, J.O., Hartmann, P., Zeier, W.G., and Janek, J. (2017). Capacity fade in solid-state batteries: interphase formation and chemomechanical processes in nickel-rich layered oxide cathodes and lithium thiophosphate solid electrolytes. *Chem. Mater.* 29, 5574–5582.
142. Zhang, W., Richter, F.H., Culver, S.P., Leichtweiss, T., Lozano, J.G., Dietrich, C., Bruce, P.G., Zeier, W.G., and Janek, J. (2018). Degradation mechanisms at the  $\text{Li}_{10}\text{GeP}_2\text{S}_{12}/\text{LiCoO}_2$  cathode interface in an all-solid-state lithium-ion battery. *ACS Appl. Mater. Interfaces* 10, 22226–22236.
143. Jin, Y., Li, N., Chen, C.H., and Wei, S.Q. (2006). Electrochemical characterizations of commercial  $\text{LiCoO}_2$  powders with surface modified by  $\text{Li}_3\text{PO}_4$  nanoparticles. *Electrochim. Solid State Lett.* 9, A273–A276.
144. Takahashi, K., Maekawa, H., and Takamura, H. (2014). Effects of intermediate layer on interfacial resistance for all-solid-state lithium batteries using lithium borohydride. *Solid State Ionics* 262, 179–182.
145. Ohta, N., Takada, K., Zhang, L., Ma, R., Osada, M., and Sasaki, T. (2006). Enhancement of the high-rate capability of solid-state lithium batteries by nanoscale interfacial modification. *Adv. Mater.* 18, 2226–2229.
146. Oh, G., Hirayama, M., Kwon, O., Suzuki, K., and Kanno, R. (2016). Bulk-type all solid-state batteries with 5 V class  $\text{LiNi}_{0.5}\text{Mn}_{1.5}\text{O}_4$  cathode and  $\text{Li}_{10}\text{GeP}_2\text{S}_{12}$  solid electrolyte. *Chem. Mater.* 28, 2634–2640.
147. Liang, J.-Y., Zeng, X.-X., Zhang, X.-D., Wang, P.-F., Ma, J.-Y., Yin, Y.-X., Wu, X.-W., Guo, Y.-G., and Wan, L. (2018). Mitigating interfacial potential drop of cathode-solid electrolyte via ionic conductor layer to enhance interface dynamics for solid batteries. *J. Am. Chem. Soc.* 140, 6767–6770.
148. Tian, Y., Shi, T., Richards, W.D., Li, J., Kim, J.C., Bo, S.-H., and Ceder, G. (2017). Compatibility Issues between electrodes and electrolytes in solid-state batteries. *Energy Environ. Sci.* 10, 1150–1166.
149. Tang, H., Deng, Z., Lin, Z., Wang, Z., Chu, I.H., Chen, C., Zhu, Z., Zheng, C., and Ong, S.P. (2018). Probing solid-solid interfacial reactions in all-solid-state sodium-ion batteries with first-principles calculations. *Chem. Mater.* 30, 163–173.
150. Liu, W., Guo, R., Zhan, B., Shi, B., Li, Y., Pei, H., Wang, Y., Shi, W., Fu, Z., and Xie, J. (2018). Artificial solid electrolyte interphase layer for lithium metal anode in high-energy lithium secondary pouch cells. *ACS Appl. Energy Mater.* 1, 1674–1679.
151. Li, N.W., Yin, Y.X., Yang, C.P., and Guo, Y.G. (2016). An artificial solid electrolyte interphase layer for stable lithium metal anodes. *Adv. Mater.* 28, 1853–1858.
152. Miara, L.J., Suzuki, N., Richards, W.D., Wang, Y., Kim, J.C., and Ceder, G. (2015). Li-ion conductivity in  $\text{Li}_9\text{S}_3\text{N}$ . *J. Mater. Chem. A* 3, 20338–20344.
153. Li, Y., Sun, Y., Pei, A., Chen, K., Vailionis, A., Li, Y., Zheng, G., Sun, J., and Cui, Y. (2018). Robust pinhole-free  $\text{Li}_3\text{N}$  solid electrolyte grown from molten lithium. *ACS Cent. Sci.* 4, 97–104.
154. Eshetu, G.G., Judez, X., Li, C., Bondarchuk, O., Rodriguez-Martinez, L.M., Zhang, H., and Armand, M. (2017). Lithium azide as an electrolyte additive for all-solid-state lithium-sulfur batteries. *Angew. Chem. Int. Ed.* 56, 15368–15372.
155. Park, K.H., Oh, D.Y., Choi, Y.E., Nam, Y.J., Han, L., Kim, J.Y., Xin, H., Lin, F., Oh, S.M., and Jung, Y.S. (2016). Solution-processable glass  $\text{Li}-\text{Li}_{14}\text{SnS}_4$  superionic conductors for all-solid-state Li-ion batteries. *Adv. Mater.* 28, 1874–1883.
156. Koerver, R., Zhang, W., de Biasi, L., Schweidler, S., Kondrakov, A.O., Kolling, S., Brezesinski, T., Hartmann, P., Zeier, W.G., and Janek, J. (2018). Chemo-mechanical expansion of lithium electrode materials – on the route to mechanically optimized all-solid-state batteries. *Energy Environ. Sci.* 11, 2142–2158.